JOURNAL OF PETROLOGY

Journal of Petrology, 2019, Vol. 60, No. 6, 1229–1262
doi: 10.1093/petrology/egz030
Advance Access Publication Date: 30 May 2019
Original Article

OXFORD

Petrology and Geochemistry of Serpentinites Associated with the Ultra-High Pressure Lago di Cignana Unit (Italian Western Alps)

Mattia Gilio [1,2]*, Marco Scambelluri[1,3], Samuele Agostini[3], Marguerite Godard[4], Daniel Peters [5,6] and Thomas Pettke[5]

[1]Dipartimento di Scienze della Terra e dell'Ambiente e della Vita, Università degli Studi di Genova, corso Europa 26, Genova, 16132, Italy; [2]Dipartimento di Scienze della Terra e dell'Ambiente, Università degli Studi di Pavia, via Ferrata 1, Pavia, 27100, Italy; [3]Instituto di Geoscienze e Georisorse, Consiglio Nazionale delle Ricerche, via Moruzzi 1, Pisa, 56124, Italy; [4]Géosciences Montpellier, Université Montpellier 2, cc60, Place Bataillon, Montpellier, 34095, France; [5]Institute of Geological Sciences, University of Bern, Baltzerstrasse 3, Bern, 3012, Switzerland; [6]Institut de Recherche en Astrophysique et Planétologie, Observatoire Midi-Pyrénées, 14 Avenue Belin, Toulouse, 31400, France

*Corresponding author. Dipartimento di Scienze della Terra e dell'Ambiente, Università degli Studi di Pavia, via Ferrata 1, Pavia, 27100, Italy. E-mail: mattia.gilio@unipv.it

Received December 1, 2017; Accepted May 26, 2019

ABSTRACT

In the Western Alps, the ophiolitic Zermatt–Saas Zone (ZSZ) and the Lago di Cignana Unit (LCU) record oceanic lithosphere subduction to high (540°C, 2·3GPa) and ultra-high pressure (600°C, 3·2GPa), respectively. The top of the Zermatt–Saas Zone in contact with the Lago di Cignana Unit consists of olivine + Ti-clinohumite-bearing serpentinites (the Cignana serpentinite) hosting olivine + Ti-clinohumite veins and dykelets of olivine + Ti-chondrodite + Ti-clinohumite. The composition of this serpentinite reveals a refertilized oceanic mantle peridotite protolith that became subsequently enriched in fluid-mobile elements (FME) during oceanic serpentinization. The olivine + Ti-clinohumite veins in the Cignana serpentinite display Rare Earth Element (REE) and FME compositions quite similar to the host-rock, which suggests closed-system dehydration of this serpentinite during subduction. The Ti-chondrodite-bearing dykelets are richer in REE and FME than the host-rock and the dehydration olivine + Ti-clinohumite veins: their Nd composition points to a mafic protolith, successively overprinted by oceanic metasomatism and by subduction zone recrystallization. These dykelets are comparable in composition to eclogites within the ultra-high pressure LCU that derive from subducted oceanic mafic crust. Different from the LCU, serpentinites from the core domains of the ZSZ display REE compositions indicating a depleted mantle protolith. The oceanic serpentinization of these rocks led to an increase in FME and to seawater-like Sr isotope compositions. The serpentinites sampled at increasing distance from the ultra-high pressure LCU reveal different mantle protoliths, still preserve an oceanic geochemical imprint and contain mafic dykelets affected by oceanic metasomatism. The subduction zone history of these rocks thus occurred under relatively closed system conditions, the only possible change during subduction being an enrichment in As and Sb recorded by the serpentinites closer to the crustal LCU. The ZSZ and Cignana serpentinites thus likely evolved in a slab setting and were weakly exposed to interaction with slab-derived fluids characteristic of plate interface settings. Our data suggest two possible scenarios for the evolution of the studied ZSZ and Cignana serpentinites. They are either part of a coherent ophiolite unit whose initial lithospheric mantle was variably affected by depletion and re-fertilization processes, or they belong to separate tectonic slices derived from two different oceanic mantle sections. In the Cignana serpentinite atop the ZSZ, the presence of Ti-chondrodite dykelets similar in composition to the LCU eclogites suggests these two domains were closely

associated in the oceanic lithosphere and shared the same evolution to ultra-high pressure conditions during Alpine subduction.

Key words: subduction; serpentinite; oceanic crust; ultra-high pressure metamorphism; fluid–rock exchange; element transfer; Lago di Cignana; Ti-chondrodite

INTRODUCTION

Serpentinites strongly impact the geochemical cycles of volatiles and fluid mobile elements (FME) and the tectonics of subduction zones (Gerya *et al.*, 2002; Deschamps *et al.*, 2013; Spandler & Pirard, 2013; Scambelluri *et al.*, 2015; Kendrick *et al.*, 2017). Their capacity to transport water (Ulmer & Trommsdorff, 1995) and mobile elements to great depths makes them like 'sponges' (Deschamps *et al.*, 2011), whose behaviour during hydration and dehydration processes affects the chemical and physical properties of both slabs and overlying mantle wedge (Rüpke *et al.*, 2004; Reynard, 2013). In the last decades, numerous studies investigated the serpentinite contribution to arc magmatism (Iwamori, 1998; Rüpke *et al.*, 2004; Scambelluri *et al.*, 2004*a*, 2004*b*, 2015, 2016; Savov *et al.*, 2005; Abers *et al.*, 2009; Deschamps *et al.*, 2011, 2013; John *et al.*, 2011; Kendrick *et al.*, 2011; Scambelluri & Tonarini, 2012; Debret *et al.*, 2013*a*, 2013*b*; Ryan & Chauvel, 2013; 2014; Cannaò *et al.*, 2015; Ribeiro & Lee, 2017) and its involvement in exhumation tectonics (Hermann *et al.*, 2000; Schwartz *et al.*, 2001). Some of these studies show that interaction with subduction fluids can variably reset the geochemical fingerprint of oceanic serpentinite (high B, U/Cs, relatively high As, Sb and marine $^{87}Sr/^{86}Sr$, $\delta^{11}B$; Kodolányi *et al.*, 2012; Peters *et al.*, 2017). These rocks are thus reliable tracers of fluid–rock interactions affecting the mantle in oceans and in subduction zones: in the latter case, geochemistry can help reconstructing the provenance of serpentinite involved in subduction tectonics and emplaced in orogens (Hattori *et al.*, 2005; Deschamps *et al.*, 2011, 2013; Scambelluri & Tonarini, 2012; Lafay *et al.*, 2013; Cannaò *et al.*, 2015, 2016; Scambelluri *et al.*, 2015; Peters *et al.*, 2017).

Increasing importance is now given to the interface between converging plates, where serpentinite is either part of large tectonic slices and/or mélanges atop the slab (Bebout, 2007; Angiboust *et al.*, 2014; Scambelluri *et al.*, 2014; Guillot *et al.*, 2015; Cannaò *et al.*, 2016), or derives from hydration of supra-subduction zone mantle (Guillot *et al.*, 2001; Bostock *et al.*, 2002; Savov *et al.*, 2005; Ryan & Chauvel, 2013), This implies complex geometries with strain localization in 100–500 m thick serpentinite shear zones enveloping less deformed bodies of oceanic mantle, crust and metasediments (Guillot *et al.*, 2001; Angiboust *et al.*, 2011, 2012*b*, 2012*c*, 2014). Understanding geometries and geochemical exchange processes in such settings helps to unravel the timing of coupling–decoupling of different oceanic slices and their accretion at the plate interface. These processes can be tackled by defining an origin (slab, supra-subduction zone mantle?) of rocks tectonically accreted to the subduction interface and, for this purpose, the serpentinized mantle rocks can provide important information (Scambelluri & Tonarini, 2012; Deschamps *et al.*, 2013; Cannaò *et al.*, 2016; Peters *et al.*, 2017).

The ophiolitic domains in the Western Alps are a well-known fossil subduction zone, where large slices of serpentinized mantle were tectonically accreted along the subduction interface at various evolutionary stages (Angiboust *et al.*, 2012a; Cannaò *et al.*, 2016). The trace element and isotopic composition of these serpentinites can display an anomalous increase in As, Sb, Pb and in radiogenic Sr and Pb above standard seawater levels, which points to influx of sediment and crust-derived fluids during their prograde to peak emplacement atop the slab into the subduction interface (Abers *et al.*, 2009; Scambelluri *et al.*, 2014; Cannaò *et al.*, 2015, 2016; Scambelluri *et al.*, 2019). Here we provide a petrologic and geochemical study of the high-pressure (HP) Zermatt–Saas Zone serpentinite (ZSZ; Fig. 1) and of the associated ultra-high pressure (UHP) oceanic crust of the Lago di Cignana Unit (LCU; Figs 1, 2) to constrain the subduction history of serpentinized oceanic mantle and to shed light on the formation mechanisms of the Alpine plate interface. We sampled serpentinites at increasing distance from the UHP Lago di Cignana Unit (Fig. 2), to test whether transition from the LCU into the ZSZ is accompanied by changes in *P–T* conditions and in the trace element and isotopic (Sr, Pb) composition of serpentinites. By comparing the geochemical and isotopic imprint of serpentinites near the LCU with those from core domains of the ZSZ, we aim at defining the origin of these mantle rocks within the Tethys Ocean and at testing if they behaved as closed or as open systems during subduction. This will shed light on the origin and behaviour of the ZSZ mantle rocks during subduction, on their potential setting within the Alpine subduction zone and on the possible structure of the Alpine subduction interface.

GEOLOGIC AND PETROLOGIC BACKGROUND

The Piedmont Ophiolite Nappe of the Western Alps is a remnant of the Mesozoic Piemontese Ocean subducted to HP–UHP conditions during the Alpine orogeny (Dal Piaz, 1999 and references therein). In Valtournenche (Aosta Valley, Italy), the Piemonte Ophiolite Nappe consists of a tectonic pile divided into the Combin Zone on top and the Zermatt–Saas Zone at the bottom. These HP

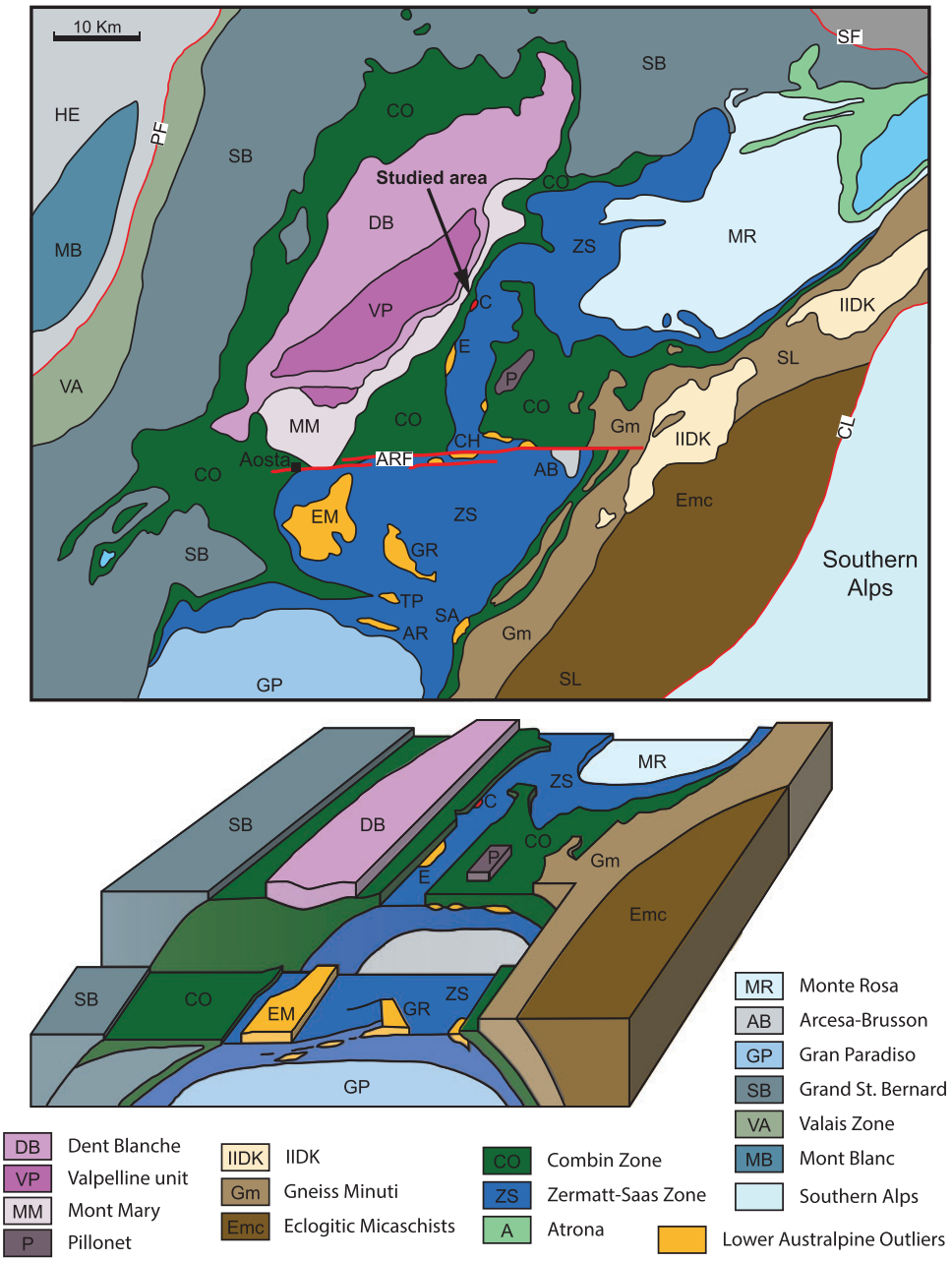

Fig. 1. Simplified geological sketch and block diagram of the Western Alps around the Zermatt–Saas Zone (redrawn after Dal Piaz *et al.*, 2001). Upper Austroalpine outliers: DB, Dent Blanche; VP, Valpelline Unit; MM, Mt. Mary; P, Pillonet; Sesia–Lanzo Inliers (SL): II–DK, Dioritic–kinzigitic; Gm, Gneiss Minuti; Emc, Eclogitic Micaschist; Inner Penninic: MR, Monte Rosa; AB, Arcesa–Brusson; GP, Gran Paradiso; Mid Penninic: SB, Grand St. Bernard; Outer Penninic: VA, Valais Zone; PF, Penninic Front; Helvetic (HE): MB, Mt. Blanc; Piemonte Zone: CO, Combin; ZS, Zermatt–Saas; A, Atrona; Lower Austroalpine Outliers: EM, Mt. Emilius; GR, Glacier–Rafray; S, Santanel; TP, Tour Ponton; AR, Acque Rosse; E, Etirol–Levaz; C, Lago di Cignana Unit; Ch, Chatillon; SV, St. Vincent; major Alpine faults: SF, Simplon Fault; CL, Canavese Line; ARF, Aosta–Ranzola Fault.

ophiolite units are underlain by the eclogite facies Mt. Rosa continental slice and are overlain by the Dent Blanche klippe (blueschist facies) and Sesia–Lanzo (eclogite facies) continental units. The Combin Unit (Fig. 1) consists of flysch-type calcschists, metamorphosed conglomerates, quartzites, dolostones and sedimentary breccias, hosting metabasic volcanoclastic layers and olistoliths (Dal Piaz, 1965; Bearth, 1967), following a lithostratigraphic sequence comparable with the non-metamorphic Northern Apennine ophiolites (External Ligurides; Elter & Pertusati, 1973). The Combin Unit equilibrated in epidote–blueschist facies during the Eocene (300–450°C and ~0·9 GPa; ~44 Ma; Reddy *et al.*, 1999). The Zermatt–Saas Zone consists of: (1) serpentinized mantle peridotite (Li *et al.*, 2004; Rebay *et al.*, 2012; Luoni *et al.*, 2018), (2) Fe–Ti and Mg–Al metagabbros and metabasalts predominantly (Bearth, 1967; Bucher *et al.*, 2005) and subordinate oceanic metasediments (Mn-rich

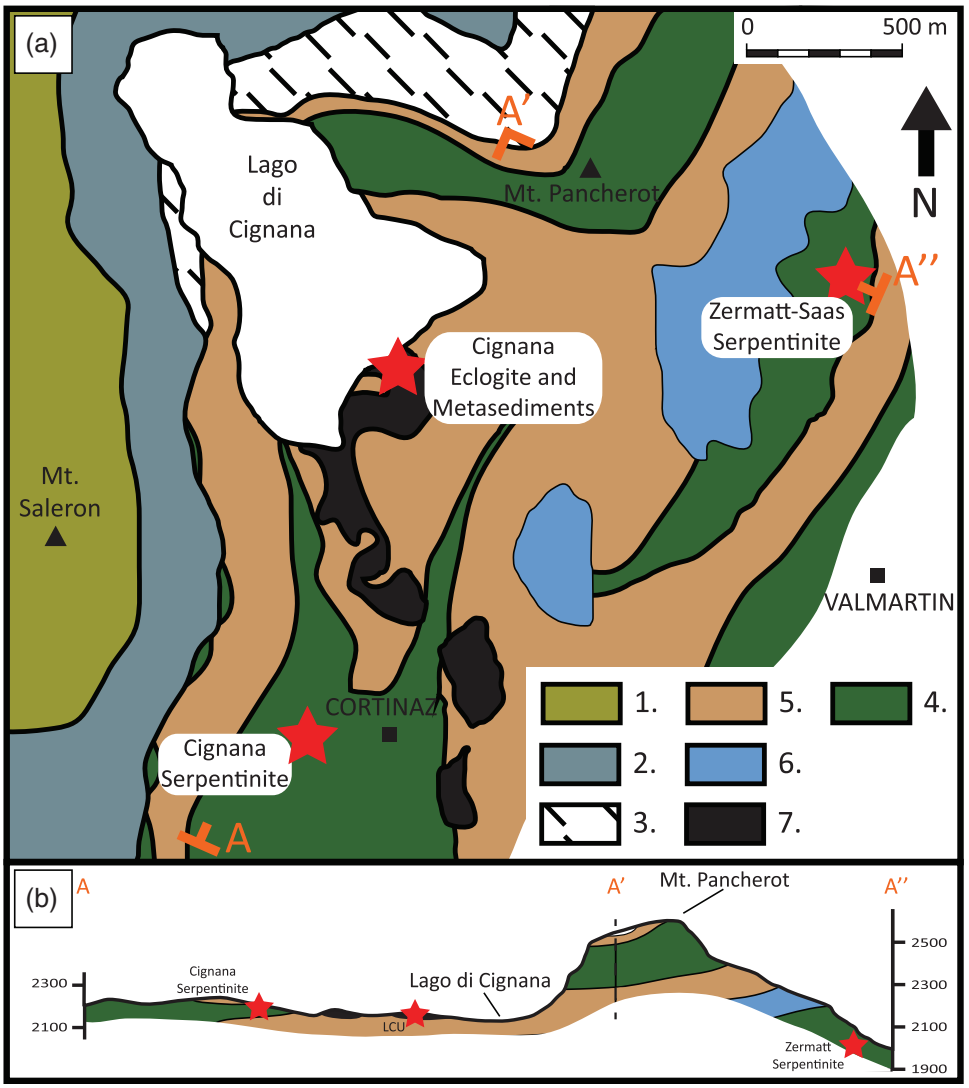

Fig. 2. Simplified geologic sketch of and profile (A–A′–A″) through the Lago di Cignana Unit, modified after Forster *et al.* (2004) and Groppo *et al.* (2009). (1) Austroalpine domain (Arolla Unit); (2) Combine Zone; (3) Pancherot Unit; Zermatt–Saas Zone: (4) Prasitites with eclogites, (5) Mg–Al metagabbros, (6) UHP Fe–Ti gabbros and metasediments of the Lago di Cignana Unit and (7) serpentinites.

quartzites, calc-schists and marbles; Dal Piaz, 1979; Bearth & Schwandler, 1981). These rocks record eclogite facies metamorphism at 520 + 20°C and 2·3 GPa and retrograde re-equilibration under blueschist and greenschist facies conditions (Angiboust *et al.*, 2009). The contact zone between the ZSZ and Combin hosts several minor bodies of continental and oceanic rocks of different age, pressure–temperature evolution and provenance (Teodulo, Etirol–Levaz, Allalin Gabbro, Cignana; Kienast, 1983; Bucher & Grapes, 2009; Beltrando *et al.*, 2010; Skora *et al.*, 2015). The ophiolitic Lago di Cignana Unit underwent Eocene subduction to > 90 km (3·2 GPa, 550°C) representing the greatest depths ever recorded by the Alpine–Himalayan oceanic crust (Fig. 1; Reinecke, 1998; Groppo *et al.*, 2009; Frezzotti *et al.*, 2011).

Previous work on Zermatt serpentinite from Valtournenche (Rebay *et al.*, 2012; Zanoni *et al.*, 2011) showed that this area records oceanic hydration and Alpine subduction, featuring three deformation events (D1, prograde; D2, peak; D3, retrograde) related to recrystallization of antigorite and metamorphic olivine. D1 develops an antigorite foliation (S1); Olivine + Ti–clinohumite + magnetite veins cut the S1 foliation and are, in turn, deformed and stretched along an olivine-bearing foliation (S2). Late crenulation (D3) and open folding deforms the pervasive HP S2 foliation and develops a weak, antigorite + chlorite foliation (S3). Zircons associated with the HP S2 foliation in serpentinite give an age of about 65·5 ± 5·6 Ma (Rebay *et al.*, 2018). Using thermodynamic modelling of Zermatt serpentinites directly underlying the Lago di Cignana Unit, Rebay *et al.* (2012) report peak pressure estimates of 2·7 GPa. Luoni *et al.* (2018) recently attributed formation of Ti-chondrodite-bearing assemblages in the ZSZ serpentinite to a stage of UHP metamorphism; a similar conclusion was proposed by Zanoni *et al.* (2016), who suggested that the

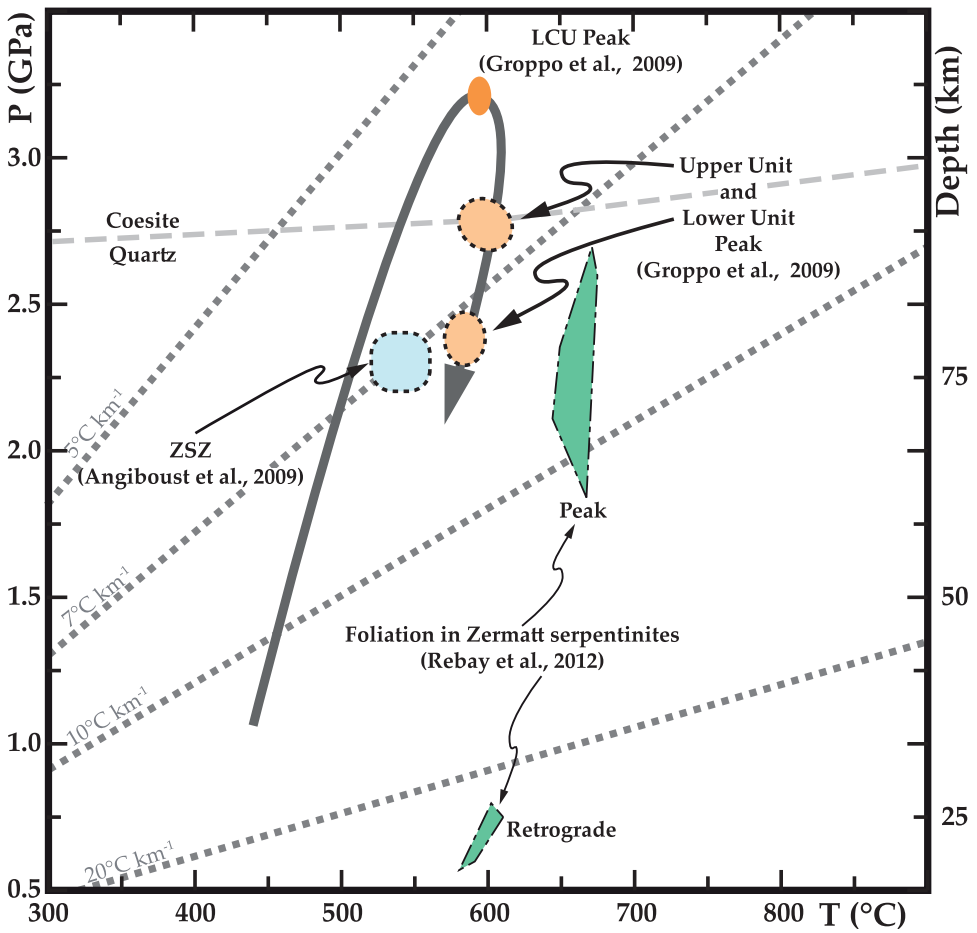

Fig. 3. *P–T* path for the Lago di Cignana Unit after Groppo *et al.*, 2009 and geothermobarometric estimates for the Zermatt–Saas Zone eclogites (Angiboust *et al.*, 2009; Groppo *et al.*, 2009) and serpentinites (Rebay *et al.*, 2012).

ZSZ is a composite tectonic slice that contains an UHP domain recording higher pressure conditions than the rest of the ZSZ unit. However, geochemical characterization of serpentinite from Zermatt–Saas and around the UHP Cignana unit has not been made.

Most of the ZSZ shows concordant peak metamorphic conditions (Fig. 3; Angiboust *et al.*, 2009) and ages (41–38 Ma, Skora *et al.*, 2015). However, near the contact with the Combin Unit there is greater complexity. Here, oceanic and continental slices of different provenance, *P–T* histories, and metamorphic ages occur within olivine– and Ti-clinohumite-bearing serpentinites (Etirol–Levaz: Kienast, 1983; Beltrando *et al.*, 2010; Pfulwe: Skora *et al.*, 2015; Allalin Gabbro: Bucher & Grapes, 2009; Teodulo Glacier Unit: Weber & Bucher, 2015; Lago di Cignana Unit: Reinecke, 1998; Groppo *et al.*, 2009; Frezzotti *et al.*, 2011). The Lago di Cignana Unit, cropping out south of the Cignana artificial lake, is one of these slices. Cignana is a small slice made of eclogite, deriving from MORB-type oceanic mafic crust, associated with oceanic sediments; it is tectonically sandwiched between the lower ZSZ and the overlying Combin and Dent Blanche Units (Reinecke, 1991; Reinecke, 1998). The peculiar feature of the Cignana crustal section is that it equilibrated under ultra-high pressure (UHP) conditions during the Alpine event (600°C, 3·2 GPa; Fig. 3; Reinecke, 1998; Groppo *et al.*, 2009), witnessed by the presence of coesite inclusions in mafic rocks and metasediments (Reinecke, 1991; 1998; Frezzotti *et al.*, 2011 and of microdiamonds in meta-sediments (Reinecke, 1991; 1998; Frezzotti *et al.*, 2011). Pressure estimates of up to 3·6 GPa derive from microdiamond occurrence (Frezzotti *et al.*, 2011). U–Pb zircon ages of the Cignana eclogite yield an average of 44·1 ± 0·7 Ma, interpreted to date the peak subduction event (Rubatto *et al.*, 1998). Rb–Sr cooling ages on white mica in Cignana metasediments indicate rapid exhumation at ~38 Ma (Amato *et al.*, 1999). Based on the Lu–Hf ages of rocks from different domains of the ZSZ, Skora *et al.* (2015) suggested that the structurally higher parts of this unit (Lago di Cignana, Pfulwe, Chamois) record peak subduction ages of 50 Ma, i.e. older than the 43–39 Ma peak subduction age of the remaining core portion of the ZSZ.

ANALYTICAL METHODS

Bulk-rock major element concentrations were measured either by XRF at the Activation Laboratories in

Toronto, Canada, or by the laser-ablation ICP-MS nanoparticulate pressed powder pellet (LA-ICP-MS-PPP) technique at the University of Bern, Switzerland (Peters & Pettke, 2017). Trace element measurements were done either by liquid-mode ICP-MS at the University of Montpellier, France, or by LA-ICP-PPP at the University of Bern, Switzerland. The use of two different analytical methods arises for: 1) validating the new LA-ICP-PPP method recently developed by Peters & Pettke (2017) and 2) analysing key trace elements in serpentinite (e.g. B), often not available from liquid ICP-MS data due to incomplete sample dissolution (e.g. zircon or chromite) or polyatomic interferences resulting from the dissolution acids employed (e.g. $(^{35}Cl^{40}Ar)^{+}$ on $^{75}As^{+}$). Data are reported and compared in Table 2. For example, the solution trace element data shows lower Zr and Hf concentrations with respect to LA-ICP-PPP, in eclogites and metasediments, indicating incomplete solution of a Zr+Hf-rich phase (likely zircon), or sub-μg/g concentrations of As are overestimated in liquid ICP-MS data.

Liquid mode ICP-MS followed the procedures described in Ionov *et al.* (1992) and in Godard *et al.* (2000). 100 mg powdered sample aliquots were dissolved in a $HF/HClO_4$ mixture in screw-top Teflon beakers and then diluted for measurement by a factor of 1000, 2000 and 4000 for ultramafic, mafic and silicic rocks, respectively, using an Agilent 7700X quadrupole ICP-MS. External calibration solutions employed were multi-element standard solutions (Merck) except for Nb and Ta, and In and Bi were used as internal standards. To avoid memory effects due to the introduction of concentrated Nb–Ta solutions into the instrument, Nb and Ta concentrations were determined by using, respectively, Zr and Hf as internal standards. This surrogate calibration technique is adapted from the method described by Jochum *et al.* (1990) for the determination of Nb by spark-source mass spectrometry. Scandium, V, Mn, Co, Ni, Cu, Zn and As were measured in helium cell gas mode, to reduce polyatomic interferences. Reproducibility and accuracy of analyses were monitored by measuring, as unknowns, the standards BHVO-1, BE-N and OU6 (used for trace-element rich rocks, such as gneiss, micaschist and black-wall), BIR-1 and MRG1 (for intermediate mafic rocks), and UB-N, JP-1 and DTS-1 (for depleted chlorite harzburgite).

Bulk-rock measurements performed by LA-ICP-MS-PPP follow the procedures documented in detail by Peters & Pettke, 2017. The sample processing procedure comprised the following steps: (1) dry milling of crushed rock powder; (2) subsequent wet milling of ~2·2 g of rock powder in 5·6 g of high purity water, all in agate milling equipment using a Retsch PM 100 planetary ball mill, to obtain an average powder grain size of a few μm; (3) the sample suspension was then dried down on a hot plate under a fume hood at 70°C; (4) the production of the pressed powder pellets involves homogenization of the dried powder and mixing by hand of 120 mg rock powder with 30 mg of microcrystalline cellulose as binder, using a small agate mortar and pestle and then pressing robust pellets in a manual hydraulic press at 500 MPa using an in-house built steel apparatus. The resulting pellets were measured at 6 spots each with a laser beam size of 120 μm, an energy density of 5 J/cm^2 at a repetition rate of 10 Hz, and calibrated by bracketing standardisation employing the United State Geological Survey (USGS) basalt glass GSD–1G. LA-ICP-MS measurements were done using a Geolas Pro 193 nm ArF excimer laser coupled with an Elan DRC-e ICP-MS at the University of Bern, Switzerland. Instrument optimisation procedures followed those detailed in Pettke *et al.* (2012). Data reduction employed SILLS (Guillong *et al.*, 2008), and 100 wt % minus LOI (wt %) was used as the internal standard for quantification. Due to lack of data on Fe^{3+}/Fe^{2+}, total iron was calculated as FeO. Analytical accuracy was monitored by measurement of BCR–2 and MUH-1 standard as PPP, and data correspond to the long-term averages reported in Peters & Pettke (2017), except for Be and Cd, for which measurements near the respective limits of detection can produce strong overestimates (Peters & Pettke, 2017).

Radiogenic isotope ratio measurements were performed at IGG-CNR of Pisa (Italy), using a Finnigan MAT 262 multiple collector thermal ionisation mass spectrometer (TIMS) for Sr and Pb, and a Thermo Neptune Plus Multi-Collector ICP-MS for Nd. For Pb, the instrument was operated in static mode. Lead fractions were purified with conventional ion chromatography using Dowex AG1-X8 anion resin, using standard HBr and HCl elution procedures. Lead was loaded on single Re (99·999% pure) filaments with TEOS solution and measured at a pyrometer-controlled temperature of 1310°C. Replicate analyses of Pb standard SRM981 yielded isotope ratios that are accurate to within 0·025% (2SD) per mass unit, after applying a mass bias correction of 0·15 ± 0·01% per mass unit relative to the NIST SRM 981 reference composition of Todt *et al.*, 1996. Lead blanks were of the order of 0·2–0·4 ng during the period of chemistry processing, hence no blank correction was made. Strontium isotope ratio measurements were performed in dynamic mode. Strontium fractions were purified using Sr-spec ion exchange resin. Instrumental mass fractionation was corrected by internal normalisation of $^{87}Sr/^{86}Sr$ according to the IUPAC value of $^{87}Sr/^{86}Sr = 0·1194$ (Meija *et al.*, 2016). Replicate measurements of the NIST SRM 987 ($SrCO_3$) standard gave an average value of 0·710207 ± 13 (2SD, n = 47). Data are corrected for inter-laboratory bias by matching the SRM987 value to $^{87}Sr/^{86}Sr = 0·710248$ (McArthur *et al.*, 2001). Throughout the full chemical process, the Sr blanks were approximately 0·3 ng, which are negligible for the analysed samples (0·3–0·5 g of sample, depending on Sr content). Nd was purified from the matrix in a two steps process, first collecting REE eluates from conventional cation columns equipped with AG 50 W-X8 200–400 mesh resin, and then extracting Nd from other REE using Eichrom Ln resin. Nd eluates were dried, then dissolved in 2% HNO_3 solution and measured in

Table 1: Studied samples and their mineral assemblages from the Lago di Cignana Unit (LCU) and from the Cignana and Zermatt (ZSZ) serpentinites

	Sample Name	Rock Type	Peak metamorphic assemblage	GPS coordinates	
				Northing	Easting
LCU	LCG1401	Eclogite	Omp, Grt, Rt, Pg	5081691	390860
	LCG1414	Quartzite	Qz, Grt, Ph, Ep	5081468	390669
	LCG1415A	Quartzite	Qz, Tur, Grt, Ph, Ep	5081468	390669
	LCG1416A	Calcschist	Cal, Qz, Grt, Ph, Ep, Pg	5081405	390653
	LCG1416B	Calcschist	Cal, Qz, Grt, Ph, Ep, Pg	5081405	390653
	LCG1501	Impure marble	Cal, Qz, Grt, Ph, Ep, Pg	5081405	390653
Cignana serp.	ZSG1402	Ti-chondrodite vein	Ti-Chn, Ti-Chu, Ap, Ol, Chl, Di, Ilm, REE-phases	5080411	390635
	ZSG1502 V	Ti-clinohumite vein	Ti-Chu, Ol, Chl, Di, Ilm, Mag, Atg	5079863	390554
	ZSG1507 V	Ti-clinohumite vein	Ti-Chu, Ol, Chl, Di, Ilm, Mag, Atg	5079808	390474
	ZSG1403	Serpentinite	Atg, Ol, Di, Chl, Mag	5080411	390635
	ZSG1502 S	Serpentinite	Atg, Ol, Di, Chl, Mag	5079863	390554
	ZSG1507 S	Serpentinite	Atg, Ol, Di, Chl, Mag	5079808	390474
	ZSG1510	Serpentinite	Atg, Ol, Di, Chl, Mag	5079908	390620
ZSZ	ZSG1405	Serpentinite	Atg, Ol, Di, Chl, Mag	5070553	395494
	ZSG1406	Serpentinite	Atg, Ol, Di, Chl, Mag	5070553	395494
	ZSG1410	Serpentinite	Atg, Ol, Di, Chl, Mag	5081230	392593

static mode with a Thermo Neptune Plus, MC-ICP-MS, equipped with 10^{11}- and 10^{12}-Ohm resistors. Blanks were negligible, thus no blank correction was performed, ^{144}Sm interference over ^{144}Nd was calculated using ^{147}Sm, however this correction also had a negligible effect on the final ratio. Instrumental mass fractionation was corrected by internal normalisation of $^{143}Nd/^{144}Nd$ according to the IUPAC value of $^{146}Nd/^{144}Nd = 0{\cdot}7219$ (Meija *et al.*, 2016). Seventeen replicates of the standard J Nd Replicate analyses of JNdi-1 standard (Tanaka *et al.*, 2000) gave an average value of $0{\cdot}512098 \pm 6$ (2SD).

In situ major element (SiO_2, TiO_2, Al_2O_3, Cr_2O_3, FeO, MgO, MnO, CaO, NiO, Na_2O and K_2O) compositions of minerals (Tables 4–6) were measured using a JEOL JXA 8200 Superprobe equipped with five wavelengths dispersive (WDS) spectrometers, an energy dispersive (EDS) spectrometer, and a cathodoluminescence detector (accelerating potential 15 kV, beam current 15 nA), operating at the Dipartimento di Scienze della Terra, University of Milano. The measurements of all elements were performed with a 30 second counting time.

RESULTS

Petrography and microstructures

We sampled HP and UHP rocks along a profile from the internal part of the ZSZ into the LCU unit (see Fig. 2 and Table 1). The tectonic units sampled include: (1) the HP serpentinite from the Zermatt–Saas Zone, in the area described in Rebay *et al.* (2012); (2) the Lago di Cignana UHP Unit (basaltic eclogite and metasediment); and (3) the serpentinite directly in contact with the UHP Lago di Cignana Unit, referred to here as the Cignana serpentinite, together with Ti-clinohumite and Ti-chondrodite-bearing dykelets within this serpentinite.

Zermatt–Saas Zone serpentinite

The Zermatt–Saas Zone serpentinite crops out in a structurally lower area with respect to the Lago di Cignana Unit (Fig. 2); three samples of Zermatt serpentinite (ZSG1405, ZSG1406, ZSG1410) were investigated in detail. The samples display a well-developed antigorite (Atg) + olivine (Ol) + diopside (Di) ± magnetite (Mag) foliation (S2) that is parallel to boudinaged rodingite dykes and deforms an earlier (S1?) antigorite foliation and/or wraps around less deformed serpentinite domains. This S2 foliation and the less deformed serpentinite include pre-kinematic clasts of former mantle clinopyroxene (Cpx), overgrown by bastite and/or metamorphic diopside, and relicts of mesh textured serpentine + magnetite after mantle olivine (Fig. 4a, b). Aggregates of metamorphic diopside are stretched along the main foliation or replace former mantle clinopyroxene porphyroclasts. Sample ZSG1406 contains fragments of olivine + Ti-clinohumite (Ti–Chu) veins, locally showing tiny Ti-chondrodite (Ti–Chn) relict grains (Fig. 4c).

Lago di Cignana eclogite and metasediments. We studied five metasediment samples comprising metaquartzite (LCG1414, LCG1415), calcschist (LCG1416A, LCG1416B) and marble (LCG1501), in addition to one basaltic eclogite (LCG1401; Table 1).

The eclogite LCG1401 (Fig. 5a) consists of garnet (Grt), omphacite (Omp), paragonite (Pg), and rutile (Rt). Garnet has inclusion-rich cores, mostly coesite (Coe; identified by Raman spectroscopy), quartz (Qz), phengite, zircon (Zrn), rutile and apatite (Ap), and inclusion-poor rims. Omphacite occurs as large (mm-sized) crystals, generally zoned from core to rim. The eclogite shows various degrees of re-equilibration along an incipient foliation defined by blue- and/or greenschist facies minerals, mostly glaucophane (Gln) after omphacite and chlorite (Chl) and barroisite (Brs) after garnet. Amongst the collected eclogites, sample

Table 2: Major (wt %) and trace element (μg/g) composition of eclogite and metasediments from the Lago di Cignana Unit, Cignana serpentinites and Ti-bearing veins, and of Zermatt serpentinite. Samples were analysed for major elements (d.l. = 0·01 wt %) and V (d.l. 5 μg/g), Be, Sr, Zr (d.l. 2 μg/g), Sc, Y, and Ba (d.l. 1 μg/g) by Fusion-ICP-MS at Act-Lab, Canada. Trace elements were analysed by liquid ICP-MS at Geosciences Montpellier (France). Detection limits (d.l.) can be found in Godard *et al.* (2000). All samples were analysed for major and trace elements by PPP-LA-ICP-MS at the University of Bern

	Lago di Cignana Unit																
	Eclogite			Quartzite						Calcschist							
	LCG1401			LCG 1414B			LCG 1415A			LCG 1416A			LCG 1416B			LCG 1501	
	FUS	ICP	PPP	FUS	ICP	PPP	FUS	ICP	PPP	FUS	ICP	PPP	FUS	ICP	PPP	PPP	
SiO_2	46·89		49·18	78·28		79·36	71·24		72·43	33·96		37·46	49·45		51·11	29·69	
TiO_2	2·49		2·37	0·219		0·23	0·454		0·44	0·131		0·14	0·182		0·19	0·1	
Al_2O_3	15·77		14·55	7·44		6·96	11·73		10·96	3·38		3·12	4·77		4·36	2·59	
Fe_2O_3(T)	10·65		10·55	4·15		3·99	5·18		4·96	1·79		1·85	2·12		2·14	1·6	
MnO	0·173		0·17	3·679		3·37	0·234		0·24	0·371		0·38	0·424		0·44	0·39	
MgO	6·07		5·83	1·17		1·14	1·8		1·72	0·81		0·95	0·8		0·82	0·94	
CaO	12·38		12·09	1·78		1·68	2·45		2·45	33·87		30·5	22·32		21·17	30·46	
Na_2O	4·75		4·53	0·23		0·27	0·65		0·65	0·19		0·18	0·23		0·21	0·09	
K_2O	0·03		0·0356	1·09		1·03	2·63		2·53	0·61		0·54	1·01		0·91	0·46	
P_2O_5	0·73		0·69	0·06		0·0526	0·11		0·1	0·06		0·0541	0·11		0·0887	0·0324	
LOI	0·4		0·4	0·4		0·4	3·09		3·09	25·54		25·54	19·08		19·08	33·65	
Total	100·3		100·4	99·23		98·48	99·57		99·57	100·7		100·71	100·5		100·52	100	
Li		22·5	24·3		5·61	5·49		22·1	20·2		7·42	6·65		7·35	6·61	2·56	
Be	1		0·98	< 1		0·71	2		1·7	< 1		0·46	< 1		0·60	0·38	
B			2·68			14·7			365			19·3			24·5	9·69	
Sc	33	30·2	28·5	10	8·85	9·99	14	12·6	12·6	5	4·79	5·02	6	5·92	6·5	4·29	
Ti		9570	14 200		1220	1380		2440	2640		734	839		969	1140	583	
V	263	246	269	38	34·7	37·3	89	86·2	86	29	26·7	26·5	35	31·4	32·1	23	
Cr			121			41·2			68·7			36·7			32·7	32·4	
Mn		1190	1320		26 800	26 100		1710	1860		2840	2940		3200	3410	3000	
Co		27·1	30·5		40·3	38·3		32·7	32·5		15·7	16·6		19·7	20·7	13·2	
Ni		85·4	114		48	49·1		84·7	82·1		36·5	47·4		46·1	51·1	37	
Cu		14·3			4·67			52·3			369			17·4		87·3	
Zn		65·3	49·8		51·5	34·6		101	57·2		27·1	20·7		40·7	24·6	21·1	
Ga		17			7·53			16·4			5			6·6		3·53	
Ge																1·1	
As		0·70	0·23		12·5	12·8		1·89	1·38		3·73	4·13		–	0·29	0·15	
Se																0·30	
Rb		0·22	0·38		39·1	40·5		113	112		23·4	25·1		36·2	37·9	18·5	
Sr	162	152	178	14	12·1	13·7	32	29	30·8	634	605	668	265	255	292	428	
Y	42	45	38	32	31·8	28	31	28·7	25·1	20	16·7	16·6	22	19·9	19·6	13·5	
Zr	256	10·9	224	61	5·24	53·1	101	3·23	79·3	27	0·67	23·1	39	0·78	37·9	19·5	
Nb		5·93	8·26		5·2	5·11		11	10·3		2·71	3·14		3·44	3·94	1·96	
Mo			0·24			1·76			0·14			0·18			0·20	0·18	
Cd			0·13			0·088			0·10			0·072			0·052	0·032	
In																0·017	
Sn		1·52			0·99			2			0·62			2·39		0·36	
Sb		0·042	0·048		0·49	0·44		0·036	0·037		0·041	0·065		0·044	0·072	0·052	
Cs		0·027	0·03		1·91	1·93		5·92	5·86		1·07	1·14		1·73	1·79	0·76	
Ba	< 2	0·87	1·41	110	98·7	109	261	237	254	57	50·7	62·4	81	72·5	88·8	42·3	
La		8·58	8·28		20·5	18·4		28·8	27·5		13·9	13·4		16·1	16·4	10·7	
Pr		3·6	3·99		4·42	4·4		6·63	7·06		3·58	3·86		3·77	4·27	2·59	
Nd		18	19·3		17·1	17·1		26	27·5		15	16·3		15·3	17·4	11·1	
Sm		5·26	5·32		3·37	3·46		5·28	5·6		3·31	3·62		3·23	3·69	2·41	
Eu		1·76	1·98		0·79	0·81		1·12	1·21		0·79	0·87		0·76	0·89	0·56	
Gd		6·89	5·67		4·35	3·45		5·88	4·7		3·86	3·4		3·81	3·38	2·46	
Tb		1·12	0·97		0·72	0·64		0·82	0·76		0·51	0·50		0·51	0·50	0·34	
Dy		7·55	6·49		4·74	4·35		4·8	4·44		2·79	2·83		2·96	3·01	2·07	
Ho		1·67	1·32		0·94	0·84		0·97	0·87		0·52	0·5		0·61	0·57	0·39	
Er		4·71	4·14		2·42	2·32		2·57	2·43		1·32	1·41		1·57	1·71	1·09	
Tm		0·70	0·58		0·33	0·3		0·37	0·34		0·18	0·18		0·22	0·22	0·14	
Yb		4·51	3·95		2·07	1·96		2·37	2·24		1·09	1·17		1·36	1·4	0·85	
Lu		0·67	0·57		0·31	0·29		0·35	0·32		0·15	0·16		0·20	0·20	0·12	
Hf		0·32	4·45		0·30	1·36		0·11	2·02		0·028	0·53		0·030	0·94	0·45	
Ta		0·38	0·45		0·300	0·32		0·67	0·69		0·14	0·19		0·20	0·24	0·11	
W		0·88	0·33		–	0·40		–	0·76		–	0·41		–	0·63	0·17	
Tl																0·111	
Pb		0·69	0·79		2·56	2·35		6·89	6·7		23·1	23·6		13·6	12·8	17·6	
Bi			0·011			0·042			0·19			0·30			0·12	0·077	
Th		0·35	0·32		5·51	5·22		7·6	7·73		1·25	1·36		3·44	3·69	1·28	
U		0·17	0·28		0·28	0·33		0·81	1·16		0·16	0·23		0·46	0·55	0·16	

(continued)

Table 2: Continued

	Cignana Serpentinite										
	Serpentinite						Ti-chondrodite dykelet			Ti-Clinohumite vein	
	ZSG 1403			ZSG 1502S	ZSG 1507S	ZSG 1510	ZSG 1402			ZSG 1502V	ZSG 1507V
	FUS	ICP	PPP	PPP	PPP	PPP	FUS	ICP	PPP	PPP	PPP
SiO_2	38·94		40·48	40·34	40·98	39·97	35·77		37·91	37·12	42·05
TiO_2	0·064		0·065	0·04	0·06	0·06	1·537		1·54	1·2	0·66
Al_2O_3	3·13		2·79	2·89	4·55	3·43	3·65		3·33	2·45	3·06
Fe_2O_3(T)	7·6		7·59	7·34	4·8	7·29	9·5		9·06	15·63	7·41
MnO	0·098		0·0999	0·08	0·07	0·09	0·176		0·17	0·23	0·17
MgO	36		34·84	33·65	25·7	35·19	35·98		34·37	33·38	30·33
CaO	2·26		2·23	3·74	11·71	2·14	4·26		4·54	3	9·34
Na_2O	0·01		0·0186	0·05	0·1	0·06	0·02		0·0263	0·05	0·09
K_2O	< 0·01		0·0015	0·002	0·0019	0·0017	< 0·01		0·0104	0·0058	0·0039
P_2O_5	< 0·01		0·0023	0·0006	0·0006	0·0017	1		0·94	0·0041	0·0009
LOI	10·42		10·42	11·87	12·03	11·77	8·03		8·03	6·93	6·89
Total	98·53		98·54	100	100	100	99·92		99·93	100	100
Li		0·16	0·26	0·28	0·62	0·37		0·72	0·79	1·35	1·09
Be	< 1		0·73	0·11	0·39	0·12	1		0·84	0·16	0·26
B			22·3	6·45	11·1	9·83			12·5	11·5	15·7
Sc	12	12·9	11·3	16·9	19·7	14·7	13	13·7	12·3	13·2	17·4
Ti		414	390	220	331	380		8690	9230	7190	3960
V	57	64·5	59	66·2	47	70·8	73	77·7	69·4	104	42·1
Cr			2450	1880	1680	2150			1870	1520	1190
Mn		771	774	644	568	683		1360	1320	1780	1320
Co		79·7	89·4	77·4	65	88·3		91·6	103	119	86·5
Ni		1710	2060	1430	1240	1730		1510	1710	1670	1200
Cu		19·8		14·7	9·77	27·1		8·7		59·8	9·77
Zn		40·9	18·1	20·1	13·8	23·9		55·8	45·1	50·7	31·8
Ga		2·73		2·74	3·68	3·15		5·5		2·46	2·7
Ge				0·77	1·02	0·72				0·74	1·05
As		0·43	0·88	1·82	0·057	0·068		2·39	3·12	2·56	0·030
Se				0·138							
Rb		0·024	0·033	0·086	0·072	0·041		0·039	0·11	0·22	0·12
Sr	10	8·33	8·9	30·5	84·9	16·7	62	55·4	60	28·5	74·4
Y	5	4	3·74	4·3	10·6	2·6	103	108	98	4·5	8·8
Zr	4	2·81	2·33	6·24	9·58	5·4	118	106	111	8·15	3·32
Nb		1·00	0·91	0·096	0·22	0·21		52·2	55·2	3·6	1·74
Mo			0·11	0·045	0·041	0·045			0·16	0·13	0·08
Cd			0·073		0·02	0·016			<0·058	0·02	0·019
In				0·011	0·008	0·013				0·0085	0·0068
Sn		0·69		0·11	0·13	0·096		0·83		0·17	0·11
Sb		0·55	0·45	0·30	0·052	0·0093		0·23	0·26	0·25	0·031
Cs		0·0014	0·0028	0·0077	0·0061	0·0042		0·0024	0·0058	0·016	0·0042
Ba	< 2	0·39	1·01	1·73	1·31	2·07	2	1·3	1·65	3·17	1·15
La		0·60	0·56	0·49	1·12	0·18		25·3	25·4	0·58	0·87
Pr		0·18	0·19	0·21	0·5	0·08		7·74	8·22	0·23	0·41
Nd		0·72	0·72	1·05	2·61	0·47		31·8	34·3	1·13	2·16
Sm		0·23	0·22	0·37	0·96	0·20		8·42	8·84	0·36	0·76
Eu		0·08	0·081	0·14	0·34	0·075		1·58	1·65	0·14	0·29
Gd		0·37	0·33	0·56	1·38	0·31		10·9	10·1	0·57	1·11
Tb		0·077	0·069	0·097	0·25	0·058		2·13	1·97	0·10	0·2
Dy		0·60	0·53	0·69	1·76	0·42		15·8	14·1	0·71	1·47
Ho		0·14	0·13	0·16	0·39	0·094		3·76	3·23	0·16	0·32
Er		0·46	0·45	0·48	1·2	0·29		12·1	11·2	0·52	0·98
Tm		0·079	0·073	0·070	0·16	0·044		2·02	1·77	0·076	0·13
Yb		0·55	0·53	0·48	1·04	0·31		13·2	12	0·53	0·87
Lu		0·089	0·084	0·070	0·13	0·052		1·79	1·57	0·083	0·13
Hf		0·067	0·054	0·18	0·32	0·16		2·14	2·13	0·20	0·17
Ta		0·074	0·072	0·0035	0·0098	0·012		3·33	3·5	0·17	0·09
W		0·12	0·12	0·018	0·038	0·015		0·33	0·28	0·058	0·047
Tl				0·0013	0·0015	0·0013				0·0036	0·0015
Pb		0·13	0·23	0·25	0·21	0·15		0·19	0·28	0·17	0·22
Bi			0·0054	0·0059	0·0018	0·0016			0·0086	0·0022	
Th		0·12	0·11	0·032	0·10	0·029		2·06	1·91	0·057	0·078
U		0·010	0·012	0·0083	0·012	0·011		0·49	0·44	0·027	0·0092

(continued)

Table 2: Continued

	Zermatt Serpentinite								
	Serpentinite								
	ZSG 1405			ZSG 1406			ZSG 1410		
	FUS	ICP	PPP	FUS	ICP	PPP	FUS	ICP	PPP
SiO_2	39·07		40·05	36·44		38·11	39·24		40·98
TiO_2	0·02		0·0189	0·043		0·0447	0·032		0·0317
Al_2O_3	1·71		1·44	1·46		1·26	1·7		1·5
Fe_2O_3(T)	8·57		8·67	14·45		14·44	7·83		7·73
MnO	0·107		0·11	0·142		0·15	0·13		0·13
MgO	36·61		35·87	37·08		35·68	39·66		38·11
CaO	0·48		0·42	0·02		<0·00980	0·57		0·49
Na_2O	< 0·01		0·0064	< 0·01		0·006	< 0·01		0·0062
K_2O	< 0·01		0·0013	< 0·01		0·0006	< 0·01		<0·00019
P_2O_5	0·01		0·0015	< 0·01		0·0008	< 0·01		0·0018
LOI	11·98		11·98	10·62		10·62	10·56		10·56
Total	98·57		98·57	100·3		100·31	99·72		99·54
Li		0·19	0·20		0·063	0·078		0·057	0·12
Be	< 1		<0·099	< 1		<0·096	< 1		<0·083
B			7·45			21·6			51
Sc	11	12·6	10·7	10	10·9	9·9	12	12·2	11·3
Ti		126	113		268	268		190	190
V	58	63·8	59·3	45	46·8	45·5	51	54·7	53·9
Cr			2930			2770			2230
Mn		844	852		1080	1160		968	1010
Co		74·6	83·8		95·3	111		95·6	114
Ni		1510	1770		1740	2020		1880	2470
Cu		30·9			9·01			17·8	
Zn		44·3	26·7		51·3	46·5		39·3	17·9
Ga		1·73			1·35			1·37	
Ge									
As		–	0·12		0·30	0·45		–	0·049
Se									
Rb		0·014	0·028		0·016	0·017		0·012	0·016
Sr	< 2	0·31	0·30	< 2	0·33	0·32	< 2	0·32	0·34
Y	3	0·37	0·31	< 1	0·29	0·30	2	0·77	0·71
Zr	2	0·30	0·24	3	0·60	0·64	3	0·53	0·50
Nb		0·058	0·054		0·068	0·071		0·031	0·030
Mo			0·057			0·088			0·12
Cd			0·16			<0·052			<0·060
In									
Sn		0·020			0·020			0·033	
Sb		0·0086	0·021		0·071	0·073		0·006	<0·015
Cs		0·0015	0·0037		0·0006	0·0025		0·0006	<0·0031
Ba	< 2	0·067	2·11	< 2	0·096	0·46	< 2	0·114	1·78
La		0·050	0·043		0·015	0·018		0·040	0·036
Pr		0·015	0·014		0·0046	0·006		0·015	0·015
Nd		0·063	0·061		0·028	0·034		0·081	0·081
Sm		0·019	0·018		0·013	0·021		0·031	0·029
Eu		0·0052	0·005		0·0026	<0·0035		0·014	0·014
Gd		0·036	0·029		0·028	0·026		0·062	0·058
Tb		0·007	0·0062		0·0056	0·0059		0·014	0·013
Dy		0·058	0·045		0·042	0·041		0·12	0·097
Ho		0·015	0·012		0·011	0·011		0·030	0·024
Er		0·048	0·047		0·035	0·037		0·098	0·096
Tm		0·0086	0·0074		0·006	0·0056		0·018	0·016
Yb		0·067	0·055		0·045	0·038		0·14	0·12
Lu		0·013	0·011		0·0088	0·0095		0·025	0·022
Hf		0·012	0·0079		0·025	0·023		0·021	0·020
Ta		0·0036	0·0021		0·0031	0·0031		0·002	0·0012
W		0·19	0·13		0·25	0·25		0·14	0·14
Tl									
Pb		0·12	0·18		0·13	0·21		0·061	0·099
Bi			0·016			0·0044			0·0036
Th		0·0025	0·0025		0·0024	0·0022		0·002	<0·0027
U		0·0008	0·0014		0·0013	0·002		0·001	0·0019

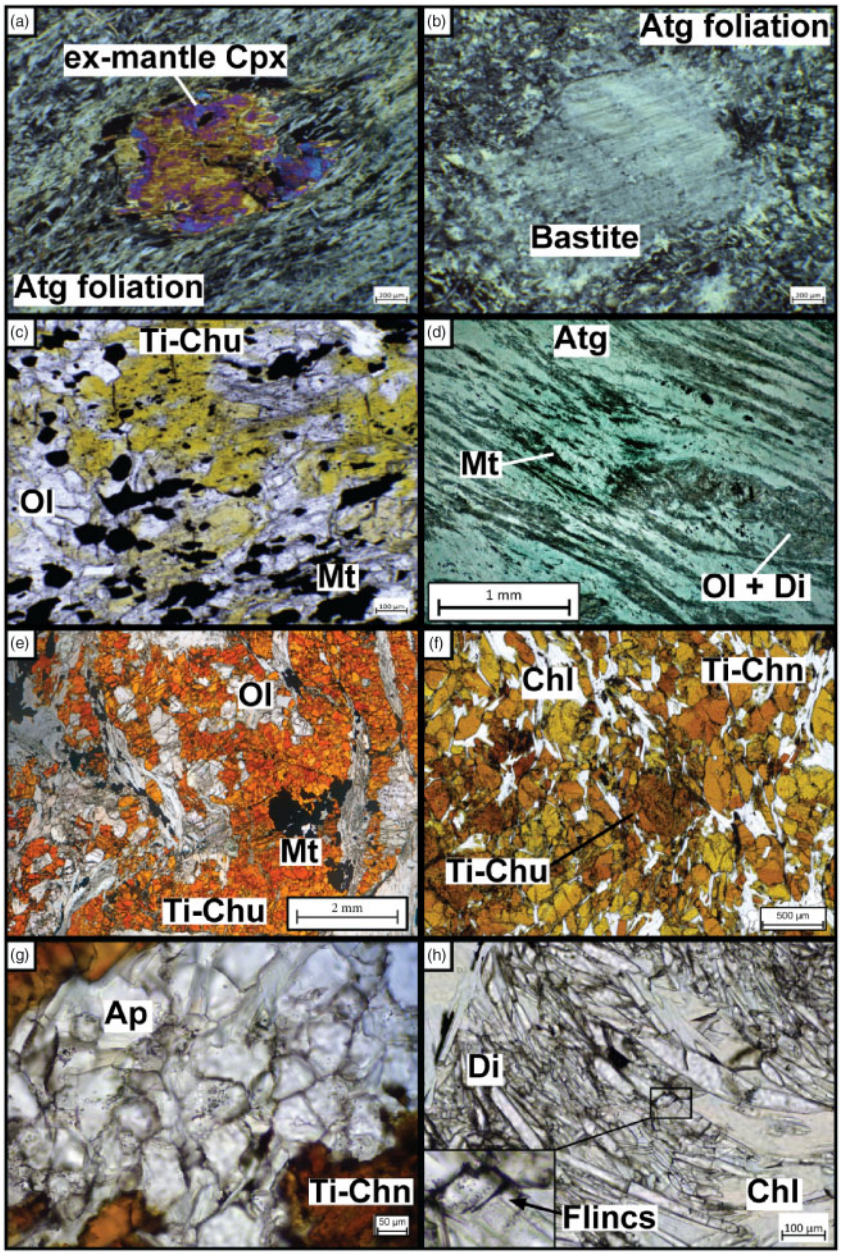

Fig. 4. (a, b, c) Microstructures of the Zermatt and (d, e, f, g, h) Cignana serpentinites and Ti-rich veins and dykelets. Zermatt serpentinite: (a) Antigorite-bearing HP foliation in the Zermatt serpentinite wrapping former mantle clinopyroxene, now overgrown by metamorphic diopside; (b) serpentinite with bastite after mantle pyroxene and serpentine + magnetite mesh structure after mantle olivine; (c) fragment of Ti-clinohumite + olivine + magnetite vein embedded in serpentinite. Cignana serpentinite: (d) Cignana serpentinite displaying a main foliation defined by elongated domains of HP metamorphic rock-forming olivine and diopside; (e) Ti-clinohumite vein hosting large (3–5 mm) crystals of olivine, Ti-clinohumite, chlorite, diopside and magnetite; (f) Ti-chondrodite dykelet. Ti-chondrodite occurs with chlorite as 0·5–1 mm–sized, isolated crystals, filled with solid inclusions of ilmenite, zircon and REE-bearing phases. Finer Ti-clinohumite crystals grow at the expense of former Ti-chondrodite; (g) mm-sized aggregates of apatite rich in solid and fluid inclusions; (h) Diopside crystals containing elongated fluid inclusions.

LCG1401 (Fig. 5a) shows the weakest retrograde overprint (< 5%).

The Cignana metasediments consist of (1): impure, locally Mn-rich, quartzite (LCG1415A, Figs 5b, c, d); (2) garnet calcschists (LCG1416A and LCG1416B, Figs 5e, f); and (3) garnet-bearing impure marbles (LCG1501). The quartzite has idiomorphic garnet and tourmaline (Tur) with inclusions of coesite, (identified by Raman spectroscopy), phengite, apatite, and rutile. Mn-quartzite contains Mn-garnet, phengite, piemontite (Pmt), pseudomorphs after lawsonite (Lws) and epidote (Ep) with allanite (Aln) cores (Figs 5c, d). Mn-garnet occurs within layers and close-packed nodules of 50–300 µm-sized crystals and often contains coesite inclusions (Fig 5d). Quartzite locally hosts large (1–2 mm) garnet crystals and zoned tourmaline (LCG1415). Oriented phengite (3T polytype; Groppo *et al.*, 2009) defines the foliation in quartzite. Quartzite is partially

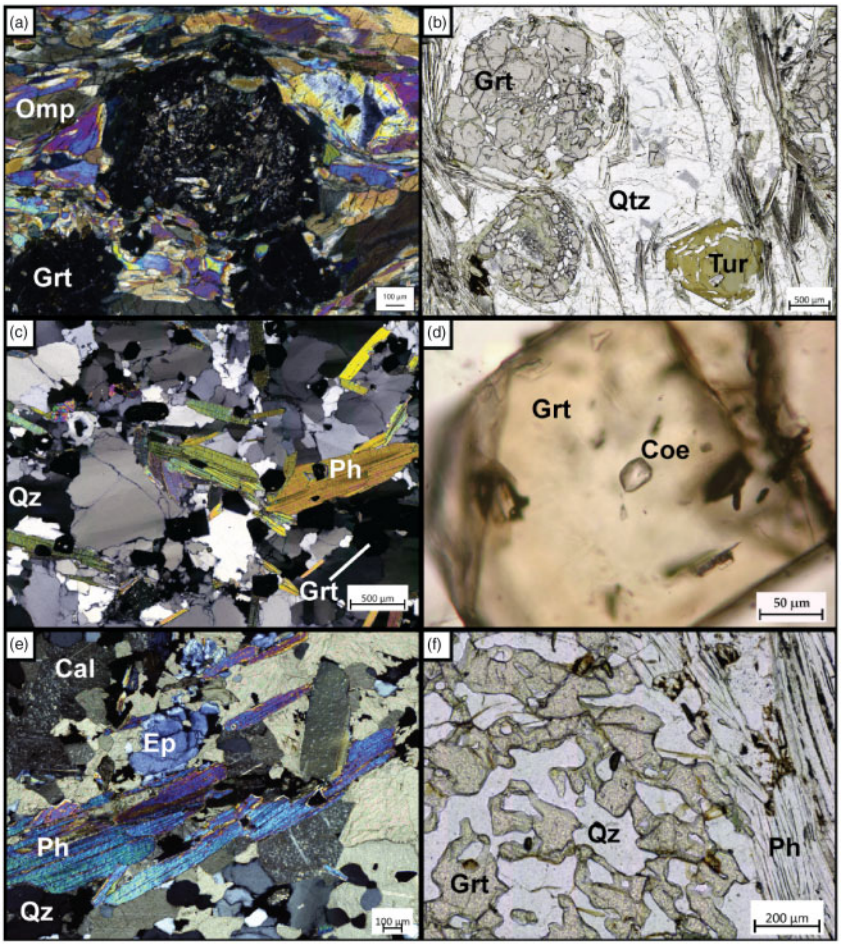

Fig. 5. Representative microstructures from the Lago di Cignana Unit. (a) Coesite-bearing eclogite. Large, inclusion-bearing garnet porphyroclasts are wrapped around by an omphacite + rutile foliation. Coesite occurs as inclusions in garnet; (b) Coesite-bearing garnet and tourmaline quartzite. Note the large poikiloblasts of garnet and tourmaline with quartz inclusions; (c) Coesite- and microdiamond-bearing garnet Mn-quartzite; (d) Coesite inclusion in garnet from Mn-quartzite; (e) Phengite, epidote and calcite from a garnet calcschist; (f) Poikilitic garnet porphyroclast with quartz inclusions in garnet calcschist.

retrogressed to epidote–greenschist facies: albite (Ab) replaces phengite, albite and muscovite (Ms) replace lawsonite, and chlorite and barroisite replace garnet. Calcschist and impure marble contain calcite (Cal), quartz, poikiloblastic garnet, epidote, phengite and rare paragonite (Figs 5e, f). Typical inclusions in garnet are calcite, apatite, rutile, coesite and white mica. The UHP eclogitic assemblage is rarely preserved in calcschists. Garnet is partially chloritized at the rims and late iron (oxy-) hydroxides replace HP mica and epidote.

Cignana serpentinite

A serpentinite body, 1 km-long and 100 m-thick, crops out 200 m west of the southern section of the Lago di Cignana Unit (Fig. 2). This serpentinite shows an antigorite + olivine-bearing HP foliation deforming rodingite dykes, comparable to the S2 foliation described for the underlying Zermatt serpentinites (Rebay *et al.*, 2012). In Cignana, widespread veins and dykelets hosting Ti-rich humite minerals cross-cut the olivine-bearing foliation (S2). We have been able to distinguish two different types of vein-like structures: Ti-clinohumite-bearing metamorphic veins and Ti-chondrodite-bearing dykelets. These rock types are quite similar based on field and textural observations, but show very different trace element and isotopic compositions, the Ti-chondrodite-bearing rock corresponding to former gabbroic material (see the following sections). Therefore, from now on we will separately consider the Ti-clinohumite metamorphic veins and the Ti-chondrodite dykelets. We investigated four serpentinite samples (ZSG1403, ZSG1502S, ZSG1507S and ZSG1510), a 1–3 cm-thick, 20 cm-long Ti-chondrodite-bearing dykelet (ZSG1402) and two Ti-clinohumite veins (ZSG1502V, ZSG1507). The S2 foliation and these veins are locally crenulated by later deformation events.

The serpentinite foliation is defined by oriented antigorite-rich layers parallel to elongated domains of HP metamorphic olivine, metamorphic diopside, and magnetite (Fig. 4d); chlorite aggregates with magnetite cores are stretched along the main foliation. Numerous Ti-clinohumite veins hosting 3–5 mm Ti-clinohumite

Table 3: Pb and Sr isotopic composition of selected samples from the Lago di Cignana Unit, the Cignana serpentinite and the Zermatt–Saas Zone serpentinite. Pb and Sr values are not corrected for their age· Neodymium isotopes are corrected both for a formation age of 165 Ma (*) and for a metamorphic age of 46 Ma (**)

		Pb						Sr		Nd		
		206/204	2σ mean	207/204	2σ mean	208/204	2σ mean	87/86	2σ mean	143/144	2σ mean	ε_{Nd}
Eclogite	LCG1401	18·55	0·003	15·52	0·002	37·99	0·006	0·70377	0·00006	0·512860*/0·512998**	0·000007	8·6*/8·3**
Tur-Quartzite	LCG1415A	18·71	0·001	15·65	0·001	38·89	0·001	0·71799	0·00006	0·512084*/0·512180**	0·000004	−8·6*/-7·6**
Calc-schist	LCG1416A	18·64	0·001	15·65	0·001	38·72	0·002	0·70943	0·00005	0·512418*/0·512162**	0·000020	−7·1*/-8·0**
Cignana Serpentinite (diopside layers)	ZSG1403	18·35	0·036	15·60	0·030	38·16	0·074	0·70423	0·00007	0·512991*/0·513008**	0·000020	11·2*/11·1**
	ZSG1502S	18·19	0·025	15·45	0·021	37·74	0·050	0·70417	0·00008	–	–	–
	ZSG1507S	18·18	0·044	15·40	0·036	37·70	0·086	0·70390	0·00004	0·512876*/0·513027**	0·000020	8·9*/8·9**
	ZSG1510	18·32	0·014	15·54	0·013	37·96	0·031	0·70394	0·00011	0·513054*/0·512150**	0·000030	12·4*/13·3**
Cignana Serpentinite (antigorite layers)	ZSG1403	18·00		15·64		37·94		0·70415	0·00004	–	–	–
	ZSG1502S	17·79		15·57		37·60		0·70486	0·00003	–	–	–
	ZSG1507S	17·88		15·55		37·68		0·70391	0·00003	–	–	–
	ZSG1510	17·73		15·56		37·57		0·70430	0·00007	–	–	–
Ti-Cho dykelet	ZSG1402	19·30	0·024	15·61	0·020	39·40	0·051	0·70422	0·00004	0·512882*/0·513008**	0·000005	9·1*/8·5**
Ti-Cl vein	ZSG1502V	18·48	0·063	15·58	0·054	38·12	0·131	0·70406	0·00015	0·512865*/0·513032**	0·000010	8·7*/9·0**
Ti-Cl vein	ZSG1507V	18·02	0·071	15·31	0·065	37·41	0·129	0·70679	0·00006	0·512932*/0·513105**	0·000020	10·0*/10·4**
Zermatt Serpentinite	ZSG1406	16·89	0·250	14·84	0·226	35·78	0·558	0·70830	0·00042	–	–	–
	ZSG1410	17·73	0·023	15·55	0·019	37·56	0·046	0·70710	0·00036	–	–	–

*corrected at 165 Ma; **corrected at 46 Ma.

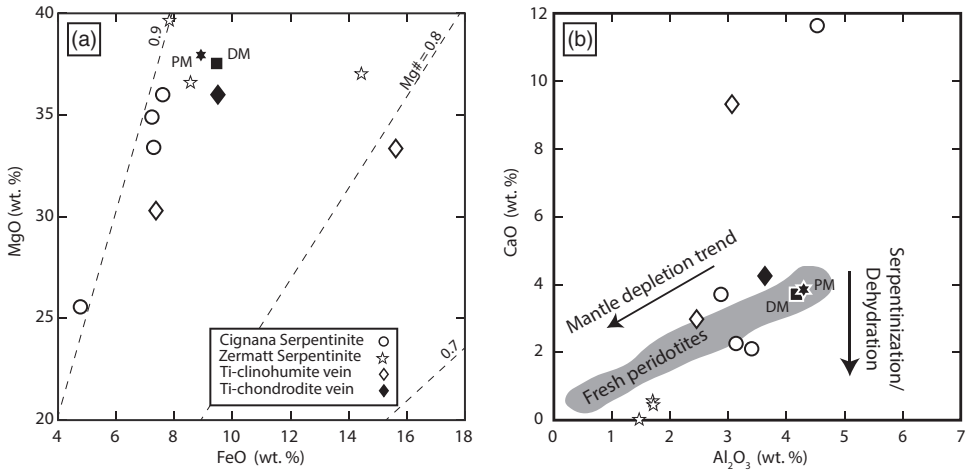

Fig. 6. Major element plots (MgO vs FeO and CaO vs Al_2O_3) for the Zermatt serpentinites and for the Cignana serpentinites and veins. MgO vs FeO: contours are Mg# = molar Mg/(Mg+Fe). CaO vs Al_2O_3: the shaded areas refer to the mantle depletion trend in peridotite.

crystals, olivine, chlorite, magnetite and rare diopside (Fig. 4e) cross-cut the olivine-bearing foliation. The ZSG1402 dykelet consists of Ti-chondrodite, chlorite, olivine, apatite and diopside (Figs 4f, g), and displays a compositional banding of 5–10 mm thick chlorite-rich rims and Ti-chondrodite-rich cores. In sample ZSG1402, Ti-chondrodite occurs as 0·5–1 mm-sized, isolated crystals, hosting inclusions of ilmenite (Ilm), zircon, baddeleyite and REE-bearing phases (Fig. 4f). Ti-chondrodite displays corroded rims, which recrystallize into 50–500 μm-sized, inclusion-free, Ti-clinohumite neoblasts (Fig. 4f). Chlorite occurs as idiomorphic, inclusion-free crystals (Fig. 4f), and apatite occurs as mm-sized aggregates of solid and fluid inclusion-rich crystals (Fig. 4g). Diopside occurs as sub-mm fibres bordering the Ti-clinohumite-rich bands (Fig. 4h). Elongated fluid inclusions occur parallel to the diopside elongation axis. Such diopside fibres extensively recrystallized into finer-grained, inclusion-free diopside crystals (Fig. 4h).

The Ti-clinohumite veins and the Ti-chondrodite-bearing sample ZSG1402 are deformed by the olivine-bearing antigorite foliation S2 and are crenulated by a later-stage deformation event (D3). Crenulations display an olivine-free, antigorite axial planar foliation. Their original mineralogy recrystallized into finer-grained (<1 mm), inclusion-free, retrograde Ti–clinohumite (2), chlorite (2) and diopside (2).

Bulk-rock compositions

The major, trace element and isotopic bulk compositions of metasediments, meta-oceanic crust and serpentinites from the Zermatt–Saas Zone and from the Lago di Cignana Unit are reported in Tables 2 and 3 and plotted in Figs 6–9.

Major elements

The Zermatt–Saas Zone serpentinite displays homogeneous harzburgitic compositions (except for the higher FeO content of sample ZSG1406) and shows much lower Al_2O_3 (~1·5–1·7 wt %) and CaO (~0·5 wt %) than the Cignana serpentinite (Figs 6a, b). The latter has a harzburgitic to lherzolitic composition, with Al_2O_3 ~2·5–4·5 wt % and CaO up to 11·6 wt %. High CaO values reflect local enrichment in modal diopside (e.g. sample ZSG1507S; up to ~40 vol. %) and likely indicates a pyroxenite component (Figs 6a, b). Ti-clinohumite veins in the Cignana serpentinite display variable major element compositions, especially regarding FeO (~7–15 wt %) and CaO (~3–9 wt %). This difference reflects the variable modal abundance in magnetite, diopside, olivine, and Ti-clinohumite. The Ti-chondrodite sample ZSG1402 has FeO, MgO, CaO and Al_2O_3 contents comparable to mantle peridotites, to the Cignana serpentinite and to the Ti-clinohumite veins (Figs 6a, b).

The Cignana basaltic eclogite (LCG1401) has Al_2O_3 ~15·8 wt %, TiO_2 ~2·5 wt % and low LOI (0·4 wt%), compatible with an altered oceanic Fe–Ti gabbro protolith, as suggested by Groppo *et al.* (2009). The Cignana metasediments include several lithological subtypes with varying silica and CO_2 contents. The most abundant varieties include quartz–micaschists with Mn-rich layers and calcschists. Quartz–micaschists have SiO_2 >70 wt % and Al_2O_3 of 7–12 wt %; their compositional variability includes high MnO (~3·7 wt %; sample LCG1414) and high B (360 μg/g; sample LCG1415) concentrations. The CaO variations in centimetre to metre-sized calcschist layers (CaO ~20–30 wt %, LOI ~20–30 wt %; LCG1416A and LCG1416B) and in silicate–marbles (CaO ~30 wt %, LOI ~35 wt %; LCG1501) reflect local variability in carbonate content.

Trace elements

Zermatt serpentinite. The Zermatt serpentinite is trace element and Rare Earth Element (REE) depleted (Figs 7, 8; normalized to C1 chondrite and PM after McDonough & Sun, 1995). The REE patterns decrease from heavy to light REE and show small negative Eu anomalies (0·2–0·4 times chondrite; Fig. 7). Nd is low, about 0·03–

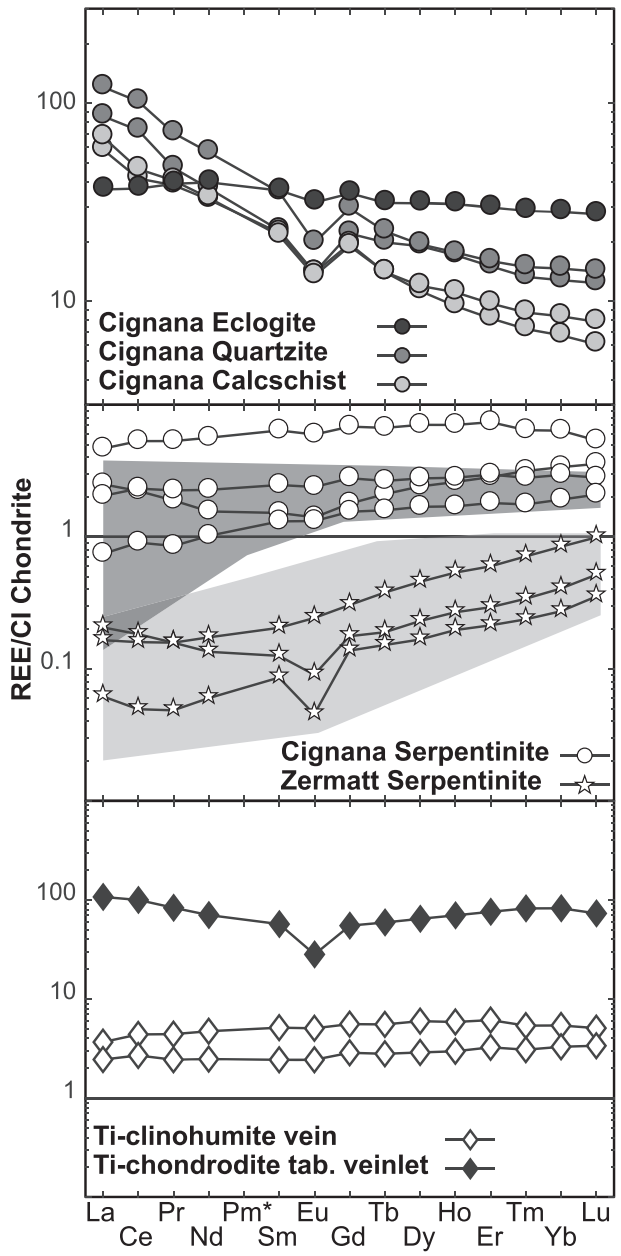

Fig. 7. CI Chondrite-normalized (McDonough & Sun, 1995) REE patterns of bulk-rock eclogite and metasediments from the UHP Lago di Cignana Unit, Cignana and Zermatt serpentinites and Cignana Ti-bearing veins and dykelet. Shaded areas are for fresh plagioclase peridotite (orange) and spinel harzburgites (blue) from the Lanzo Massif (Guarnieri *et al.*, 2012).

0·08 μg/g. All samples display comparable PM-normalized TE patterns, with enrichments in B, Bi, W, As, Sb, Be and Mo with respect to the mantle depletion trend (Fig. 8).

Cignana serpentinite. The Cignana serpentinite shows flat REE patterns, with values ranging from 1 to 10 times chondrite (Fig. 7); the Nd content ranges between 0·5–2·6 μg/g. The trace element patterns show positive anomalies in several fluid-mobile elements (Fig. 8); As and Sb, for instance, are highly variable and range from PM values (ZSG1510; 0·07 and 0·01 μg/g) up to values two orders of magnitude higher (ZSG1502S, 1·82 and 0·3 μg/g). Moreover, this serpentinite is enriched in B, Bi, W, As, Sb, Sr, Be and Th relative to the mantle depletion trend. The trace element patterns of Ti-clinohumite veins hosted by the Cignana serpentinites closely resemble those of the host-rocks, except for increased Nb, Ta and Ti. Their Nd content (1·1–2·2 μg/g) is comparable to that of the serpentinite host. In contrast, the Ti-chondrodite dykelet ZSG1402 shows up to 2 orders of magnitude higher REE (Nd = 31·8 μg/g) and trace element contents (especially Nb, Ta, Th, U) than the host serpentinite. Its heavy REE and Nd content is higher than that of the host serpentinite and of the associated Ti-clinohumite veins, and is comparable to that of the LCU eclogite. The Cs, Rb, Ba, B, Cd, Pb, As, Sb, Sr, Ga and Li contents are comparable with those of Cignana serpentinite.

LCU crustal rocks. The Cignana eclogite has a flat REE and trace element pattern (Figs 7 and 8). Except for a slight depletion in Cs, Rb, Ba, and K, all trace elements are 10 to 30 times higher than the primitive mantle, with higher enrichment in the most incompatible elements. The Nd content of this eclogite is 18 μg/g. The Cignana metasediments have homogeneous REE patterns, showing a steady decrease from light to heavy REE (Fig. 7). The Nd content of metasediments ranges between 11 and 27 μg/g. All samples display weak negative Eu anomalies. The trace element patterns show positive peaks in Cs, Rb, Pb, As and Sb and negative troughs in Cd and Ti (Fig. 8). Quartzites and calcschists show similar trends, except for Pb and Sr, which are up to one order of magnitude higher in calcschists, and for As and Sb, which are generally higher in quartzites. The remarkably high B content (365 μg/g) of sample LCG1415 reflects the presence of tourmaline.

Isotopic compositions

Selected samples of Zermatt and Cignana serpentinites and of UHP crustal rocks from the LCU were analysed for their Pb, Sr and Nd isotopic compositions. In samples ZSG1403, ZSG1502, ZSG1507 and ZSG1510 we analysed both the diopside-bearing bulk-rock and antigorite-rich layers. All results are shown in Table 3 and displayed in Figs 9a–c. We performed age corrections only on Nd isotopic data, as age corrections for Sr and Pb isotopes resulted to be less than the reported uncertainty for each measurement. The serpentinite samples, the Cignana eclogite and the Ti-chondrodite dykelet (evidence presented below shows the latter are metasomatized former mafic intrusives) have been corrected to 165 Ma (the age of the Jurassic opening of the Tethys ocean; Rubatto *et al.*, 1998; Beltrando *et al.*, 2010). The Cignana metasediments and the Ti-clinohumite veins have been corrected to 46 Ma, the age of HP metamorphism in the Zermatt–Saas Zone (Rubatto *et al.*, 1998; Beltrando *et al.*, 2010). The Zermatt serpentinite shows non-radiogenic Pb isotopic values (lower than DM values) for all three isotopic systems

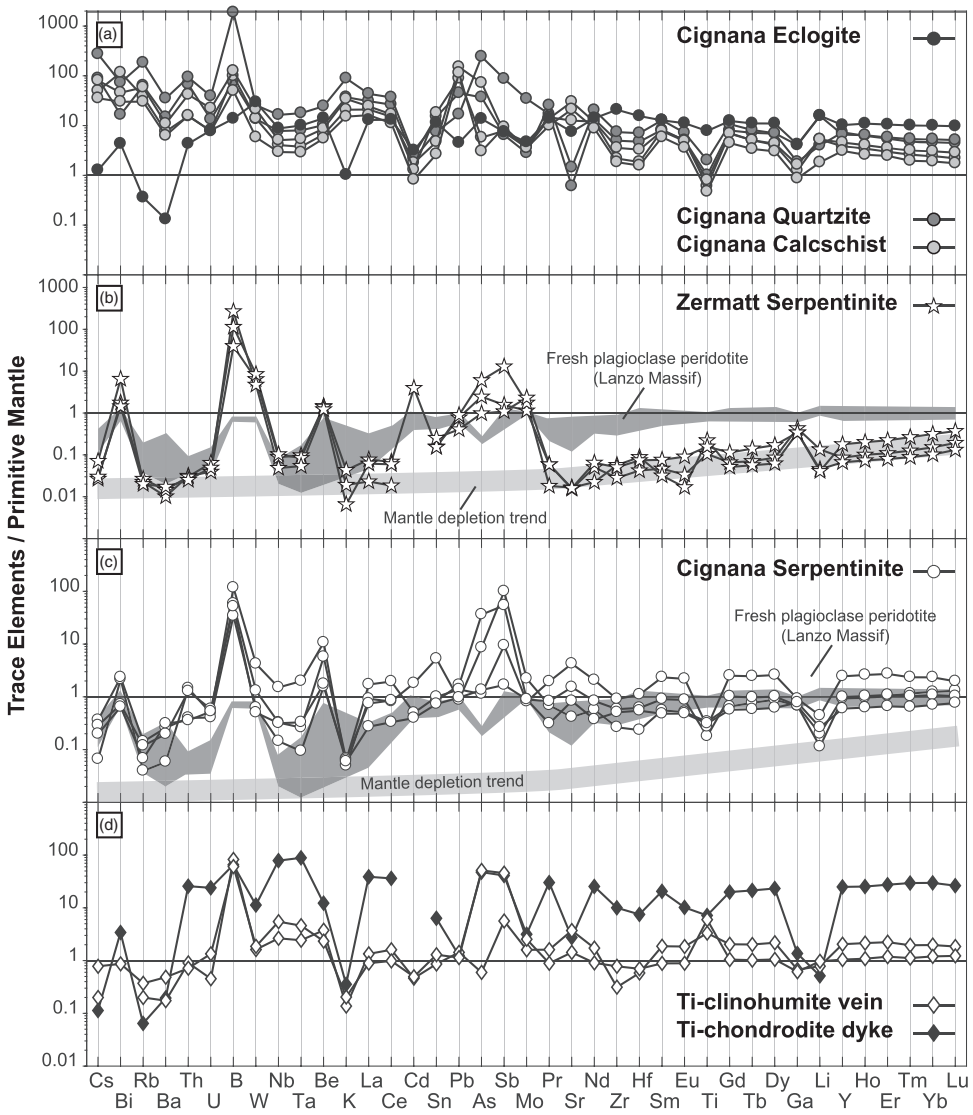

Fig. 8. PM-normalized (McDonough & Sun, 1995; B and Li after Marschall *et al.*, 2017) trace element patterns of bulk-rock (PPP data used from Table 1) eclogite and metasediments from the UHP Lago di Cignana Unit, Cignana and Zermatt serpentinites, and Cignana Ti-bearing veins. Shaded areas are for fresh plagioclase peridotite from the Lanzo Massif (orange; Guarnieri *et al.*, 2012) and the mantle depletion trend (blue).

($^{206}Pb/^{204}Pb$, $^{207}Pb/^{204}Pb$, and $^{208}Pb/^{204}Pb$ are 16·89–17·73, 14·84–15·55, and 35·78–37·56, respectively) and $^{87}Sr/^{86}Sr = 0·707051$, a value indicative of serpentinization by Jurassic seawater (Jones & Jenkyns, 2001; Vils *et al.*, 2009; Cannaò *et al.*, 2016). The Cignana eclogite shows a typical MORB isotopic composition (Kelemen *et al.*, 2003) with $^{206}Pb/^{204}Pb$, $^{207}Pb/^{204}Pb$, and $^{208}Pb/^{204}Pb$ of 18·55, 15·52 and 37·99, respectively. The eclogite also shows $^{87}Sr/^{86}Sr = 0·703764$ and $\varepsilon_{Nd} = +8·3$. The Cignana metasediments (quartzite and calcschist) are similar to the reference GLOSS-II reservoir (Plank, 2014), with $^{206}Pb/^{204}Pb$, $^{207}Pb/^{204}Pb$ and $^{208}Pb/^{204}Pb$ between 18·64–18·71, 15·64–15·65 and 38·72–38·88, respectively. $^{87}Sr/^{86}Sr$ is between 0·709368 and 0·711573 and ε_{Nd} = -8·4 to -8·1. The Cignana serpentinite has Pb isotope values between DM and MORB values ($^{206}Pb/^{204}Pb$, $^{207}Pb/^{204}Pb$, and $^{208}Pb/^{204}Pb$ are 18·17–18·34, 15·40–15·60 and 37·69–38·13, respectively), and ε_{Nd} between +8·9 and +13·6; $^{87}Sr/^{86}Sr$ is 0·703883–0·704160, lower values than Jurassic seawater (Jones & Jenkyns, 2001) and similar to MORB (Kelemen *et al.*, 2003) and the Cignana eclogite. We also analysed antigorite-rich layers from the Cignana serpentinite, showing Pb isotopic values tending towards those of the Zermatt serpentinite ($^{206}Pb/^{204}Pb$, $^{207}Pb/^{204}Pb$, and $^{208}Pb/^{204}Pb$ are 17·73–18·00, 15·55–15·64, and 37·57–37·94, respectively) and Sr isotopic values slightly higher than the ZSZ serpentinite (0·703906–0·704861). The Zermatt serpentinite and antigorite-rich layer in the Cignana serpentinite were

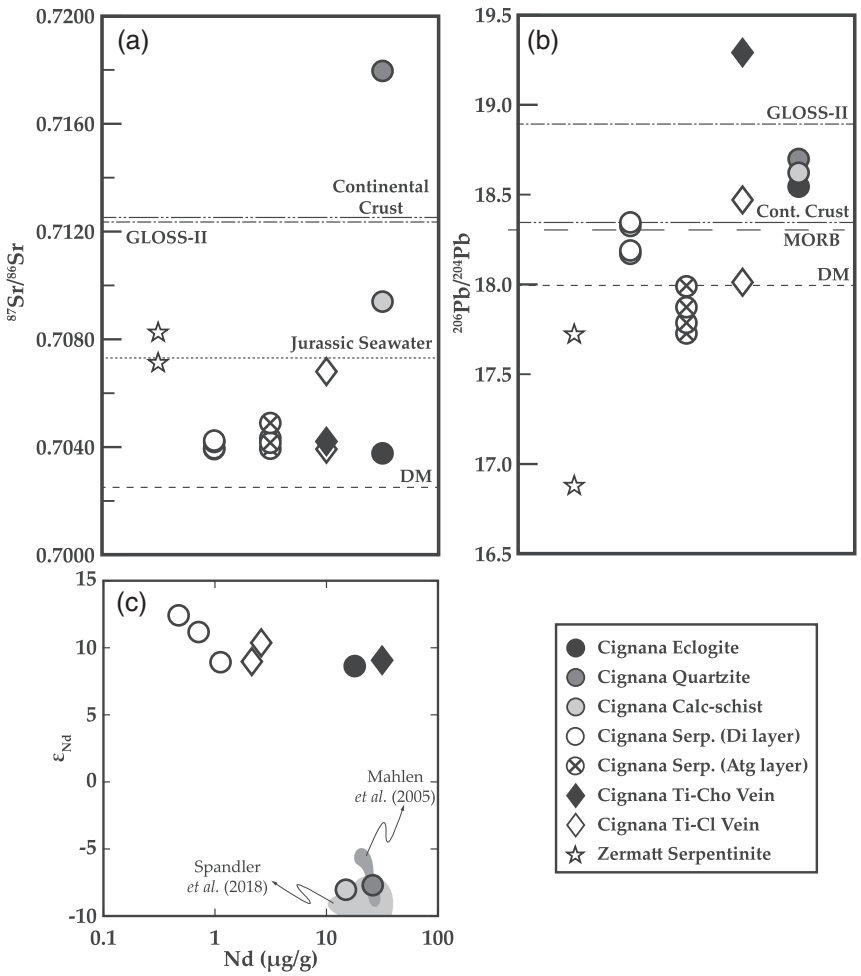

Fig. 9. $^{87}Sr/^{86}Sr$, $^{206}Pb/^{204}Pb$ and ε_{Nd} vs Nd for analysed samples from the Lago di Cignana Unit, Cignana serpentinites and veins and Zermatt serpentinites. Plotted Nd isotope compositions of serpentinites, eclogite and Ti-chondrodite dykelet are corrected for their formation age of 165 Ma, whereas the Nd isotope compositions of Ti-clinohumite veins and Cignana metasediments are corrected for their metamorphic age of 46 Ma. Values for GLOSS-II (Plank, 2014), depleted mantle (Rehka & Hofmann, 1997), Jurassic seawater (Jones & Jenkyns, 2001), MORB (Kelemen *et al.*, 2003) and average continental crust (Rudnick & Gao, 2003) and ε_{Nd} data from Mahlen *et al.*, 2005 and Spandler *et al.*, 2018 are reported for comparison.

not analysed for their Nd isotopic composition due to their low Nd contents. The Ti-clinohumite vein and the Ti-chondrodite dykelet in the Cignana serpentinites have similar $^{87}Sr/^{86}Sr$ isotope ratios, close to MORB values (0·704221 in the dykelet; 0·704059 in the veins). The Ti-clinohumite veins have Pb isotopic compositions comparable with their ZSZ and Cignana host serpentinites. In contrast, the Ti-chondrodite dykelet ZSG1402 is rich in radiogenic lead and shows values within the range reported for the Lago di Cignana UHP eclogite and metasediments. The age-corrected Nd isotope compositions of all analysed mafic and ultramafic samples (Cignana serpentinite, Ti-clinohumite veins, Ti-chondrodite dykelet and Cignana eclogite) fall in a range between ε_{Nd} 8·6 and 12·4. Considering the Nd isotopes, Fig. 9c shows a huge difference between the negative ε_{Nd} values of LCU metasediments (around -9) and the positive ε_{Nd} of the LCU eclogite (8·6), of the Cignana serpentinite (8·9–12·4) and of the associated Ti-clinohumite veins (9·0–10·4) and Ti-chondrodite dykelet (9·1). These data indicate no significant exchange between sedimentary and mafic-ultramafic rocks. Considering the bulk Nd content, Fig. 9c clearly points out the affinity between the Cignana serpentinite and its Ti-clinohumite veins, having from 0·72 to 2·16 μg/g Nd, and between the Ti-chondrodite dykelet and the LCU eclogite, with 18 to 34·3 μg/g Nd.

Mineral compositions

Major elements

We performed electron microprobe analyses of rock-forming minerals from the Zermatt serpentinite, the Ti-clinohumite veins and Ti-chondrodite veinlet hosted by the Cignana serpentinite, and the Cignana eclogite and metasediments. Representative mineral compositions are reported in Tables 4–9; the full dataset is shown in the Supplementary Data; supplementary data are available for downloading at http://www.petrology.oxfordjournals.org.

Table 4: Representative electron microprobe analyses of mineral phases from the Cignana serpentinite. Ti-clinohumite was recalculated anhydrous, assuming full site occupancy to a total of 13 apfu

	Sample 1503									
	Chlorite		Diopside		Olivine		Antigorite		Ti-Clinohumite	
SiO_2	33·60	33·59	56·01	55·29	39·99	40·10	42·17	42·22	36·15	36·36
TiO_2	0·04	0·00	0·15	0·00	0·00	0·00	0·06	0·00	4·64	4·40
Al_2O_3	12·90	12·66	0·03	0·00	0·01	0·01	2·44	2·60	0·00	0·00
Cr_2O_3	0·66	0·74	0·05	0·03	0·01	0·06	0·34	0·31	0·00	0·00
FeO	4·61	4·55	1·87	1·26	13·13	13·04	4·51	4·75	12·65	12·46
MnO	0·03	0·07	0·12	0·05	0·37	0·40	0·07	0·07	0·40	0·49
MgO	34·30	33·76	18·14	17·93	47·96	47·22	37·44	37·69	45·50	45·73
NiO	0·12	0·17	0·11	0·00	0·47	0·40	0·14	0·19	0·32	0·22
CaO	0·02	0·00	25·45	25·67	0·01	0·04	0·01	0·03	0·02	0·04
Na_2O	0·00	0·00	0·18	0·09	0·00	0·02	0·00	0·05	0·02	0·03
Totals	86·32	85·55	102·11	100·31	102·00	101·33	87·17	87·93	99·70	99·74
Si	6·435	6·495	1·989	1·996	0·974	0·984	1·982	1·972	3·959	3·973
Ti	0·006	0·000	0·004	0·000	0·000	0·000	0·002	0·000	0·382	0·362
Al	2·916	2·886	0·001	0·000	0·000	0·000	0·135	0·143	0·000	0·000
Cr	0·100	0·114	0·001	0·001	0·000	0·001	0·013	0·011	0·000	0·000
Fe(III)	0·000	0·000	0·001	0·001	0·014	0·008	0·000	0·000	0·000	0·000
Fe(II)	0·780	0·740	0·054	0·038	0·254	0·259	0·177	0·186	1·159	1·139
Mn	0·006	0·012	0·004	0·001	0·008	0·008	0·003	0·003	0·037	0·045
Mg	9·792	9·732	0·961	0·965	1·741	1·728	2·624	2·625	7·429	7·450
Ni	0·019	0·026	0·003	0·000	0·009	0·008	0·005	0·007	0·028	0·019
Ca	0·004	0·000	0·969	0·993	0·000	0·001	0·000	0·001	0·002	0·004
Na	0·000	0·000	0·012	0·006	0·000	0·001	0·000	0·004	0·004	0·006
H	16·000	16·000	0·000	0·000	0·000	0·000	4·000	4·000	0·000	0·000
Totals	36·057	36·006	4·000	4·000	3·000	3·000	8·942	8·953	13·000	13·000

*corrected at 165 Ma; **corrected at 46 Ma.

In the Zermatt serpentinite, antigorite (Fig. 10a) has low Al contents (∼0·05–0·09 a.p.f.u.) and high Mg# (∼0·97–0·98); olivine (Fig. 10b) has low NiO_2 contents (∼0·05–0·1%) and Mg# (∼0·96–0·98), comparable with associated antigorite. Ti-clinohumite and Ti-chondrodite have a Ti content of 0·2 and 0·3 a.p.f.u. respectively (Figs 10c–d).

The Cignana eclogite consists of garnet, omphacite and rutile. Garnet is almandine–grossular rich, with Fe-rich cores (Alm ∼56–57% and Prp ∼ 7%) and Mg contents increasing towards the rims (Alm ∼50–51% and Prp ∼8–9%). The jadeite content in omphacite increases from ∼50% in the core to ∼70% in the rim. Epidote occurs as small inclusions within garnet cores and has ∼50% clinozoisite component. In the Cignana quartzite, garnet is almandine–grossular and has Ca-rich cores (Alm ∼50–53%, Grs ∼27–28%, Sps ∼10–11% and Prp ∼4%). The Fe(II) content increases towards the rims (Alm ∼ 69–70%, Grs ∼ 10–11%, Sps ∼ 1–2% and Prp ∼ 16–17%). Tourmalines are dravites, with schorl contents increasing from cores (∼ 18–19%) to rims (∼ 30–31%). Mn-rich layers in quartzites consists of quartz, Mn–rich (sps > 70%) garnet, phengite, and epidote (allanite cores and clinozoisite ∼ 30% towards the rims).

In the Cignana serpentinite, antigorite (Fig. 10a) has Mg#∼0·93–0·96 and variable Al contents (0·9–0·15 a.p.f.u.). Olivine (Fig. 10b) shows similar compositions both in the serpentinites and in the Ti-clinohumite veins, having Mg#∼0·84–0·88 (one outlier at 0·81) and variable NiO_2 contents (∼0·15–0·5%). Similarly, Ti-clinohumite (Fig. 11c) has similar compositions both in the Ti-clinohumite veins and in the Ti-chondrodite dykelet (Ti∼0·3–0·5 a.p.f.u.).

Trace elements

The full LA-ICP-MS mineral trace element dataset for the Zermatt and Cignana serpentinites, their Ti-clinohumite veins and Ti-chondrodite veinlet, and for the Cignana eclogite and metasediments is reported in the Supplementary Data. Representative analyses are shown in Tables 10–13 and plotted in Fig. 11. Antigorite (Fig. 11) displays rather similar trace element and REE patterns, both in Cignana and Zermatt serpentinites. The antigorite compositions are REE-depleted (0·01 to 0·1 times C1 chondrite), showing a slight increase from light to heavy REE. The Cignana antigorite is slightly more enriched in light REE and shows enrichment in Th, Be, Ta, La and Ce. Conversely, the Zermatt antigorite has higher B, As and Sb. In the Cignana serpentinite, olivine is depleted in light REE and enriched in heavy REE, B, Sb and Li (Fig. 11). The Cignana diopside is enriched in REE (∼5–10 times C1 chondrite) and in Rb, U, Th, Be, Ce, Pb and Sr. Ti-clinohumite (Fig. 11) has generally similar patterns in all Cignana lithologies. Ti-clinohumite is enriched in Nb, Ta, B, W, As, Sb and REE with respect to Primitive Mantle (PM). Ti-clinohumite in the Zermatt serpentinite also has enriched but lower absolute levels of REE, Nb and Ta due to the overall stronger melt depletion of the bulk-rocks compared to the Cignana serpentinites. Ti-clinohumite shows enrichments of up to 200–

Table 5: Representative electron microprobe analyses of mineral phases from Ti-chondrodite and Ti-clinohumite veins hosted within Cignana serpentinite. Ti-clinohumite and Ti-chondrodite are recalculated anhydrous, assuming full site occupancy to a total of 13 and 7 apfu, respectively

	Sample 1402						Sample 1502								Sample 1507							
	Chlorite		Ti-Chondrodite		Ti-Clinohumite		Chlorite		Diopside		Olivine		Ti-Clinohumite		Chlorite		Diopside		Olivine		Ti-Clinohumite	
SiO_2	33·83	33·74	32·42	32·60	35·70	35·86	33·68	34·25	55·20	55·55	40·03	39·88	35·65	35·88	33·73	35·05	55·43	55·50	40·01	40·00	35·47	35·31
TiO_2	0·00	0·02	8·85	8·55	5·13	5·11	0·04	0·00	0·04	0·00	0·00	0·00	5·03	4·62	0·10	0·20	0·02	0·00	0·13	0·09	4·91	4·92
Al_2O_3	13·12	13·44	0·01	0·03	0·00	0·00	13·04	13·42	0·03	0·01	0·00	0·01	0·00	0·02	13·61	10·90	0·05	0·17	0·00	0·02	0·00	0·02
Cr_2O_3	0·35	0·27	0·00	0·00	0·03	0·03	0·05	0·38	0·00	0·00	0·04	0·01	0·00	0·00	0·12	0·04	0·02	0·09	0·05	0·00	0·02	0·00
FeO	4·92	4·85	12·88	12·73	12·63	12·34	5·17	5·16	1·34	1·32	13·77	13·75	13·81	13·73			1·96	2·87				
MnO	0·05	0·04	0·51	0·43	0·32	0·33	0·02	0·00	0·13	0·15	0·54	0·49	0·58	0·63	5·63	5·15	0·09	0·15	14·03	13·11	16·54	16·93
MgO	34·25	33·49	42·79	42·52	45·83	45·53	32·96	32·91	17·65	17·56	46·08	45·81	43·01	43·49	0·11	0·09	17·28	16·47	0·66	0·50	0·66	0·66
NiO	0·16	0·10	0·14	0·10	0·19	0·16	0·28	0·23	0·00	0·01	0·31	0·26	0·16	0·32	32·53	33·79	0·05	0·06	45·17	46·15	40·95	40·66
CaO	0·00	0·00	0·05	0·01	0·00	0·01	0·01	0·00	25·45	25·47	0·00	0·00	0·00	0·01	0·18	0·16	24·92	24·05	0·18	0·24	0·22	0·12
Na_2O	0·01	0·00	0·03	0·01	0·00	0·03	0·03	0·03	0·06	0·06	0·01	0·01	0·02	0·01	0·02	0·00	0·27	0·70	0·00	0·02	0·02	0·00
Totals	86·73	86·03	97·70	97·00	99·84	99·44	85·28	86·39	99·90	100·15	100·78	100·22	98·28	98·71	86·07	85·39	100·08	100·07	100·23	100·14	98·82	98·64
Si	6·452	6·481	1·986	2·010	3·904	3·939	6·531	6·544	2·003	2·009	0·992	0·994	4·003	4·003	6·491	6·779	2·010	2·017	1·000	0·996	4·014	4·009
Ti	0·000	0·002	0·408	0·396	0·422	0·422	0·006	0·000	0·001	0·000	0·000	0·000	0·425	0·388	0·014	0·029	0·000	0·000	0·002	0·002	0·418	0·420
Al	2·953	3·045	0·000	0·002	0·001	0·000	2·983	3·028	0·001	0·000	0·000	0·000	0·000	0·003	3·087	2·485	0·002	0·007	0·000	0·001	0·000	0·003
Cr	0·053	0·041	0·000	0·000	0·003	0·003	0·008	0·058	0·000	0·000	0·001	0·000	0·000	0·000	0·018	0·007	0·001	0·003	0·001	0·000	0·002	0·000
Fe(III)	0·000	0·030	0·000	0·000	0·000	0·000	0·031	0·093	0·000	0·000	0·004	0·003	0·000	0·000	0·060	0·062	0·000	0·000	0·000	0·001	0·000	0·000
Fe(II)	0·821	0·749	0·660	0·656	1·155	1·134	0·807	0·732	0·041	0·040	0·281	0·283	1·297	1·281	0·846	0·771	0·059	0·087	0·293	0·272	1·565	1·608
Mn	0·008	0·007	0·027	0·022	0·029	0·031	0·003	0·000	0·004	0·005	0·011	0·010	0·055	0·060	0·019	0·014	0·003	0·005	0·014	0·010	0·063	0·064
Mg	9·738	9·590	3·908	3·908	7·470	7·456	9·528	9·373	0·955	0·947	1·703	1·703	7·199	7·233	9·331	9·742	0·934	0·892	1·683	1·713	6·909	6·883
Ni			0·007	0·005	0·016	0·014	0·044	0·035	0·000	0·000	0·006	0·005	0·014	0·028	0·028	0·025	0·001	0·002	0·004	0·005	0·020	0·011
Ca	0·025	0·015	0·003	0·001	0·000	0·001			0·989	0·987	0·000	0·000	0·000	0·001	0·003	0·001	0·968	0·937	0·000	0·001	0·002	0·000
Na			0·000	0·000	0·000	0·000	0·002	0·001	0·004	0·004	0·000	0·000	0·004	0·003	0·024	0·003	0·019	0·050	0·000	0·000	0·005	0·000
H	16·000	16·000	0·000	0·000	0·000	0·000	16·000	16·000	0·000	0·000	0·000	0·000	0·000	0·000	16·000	16·000	0·000	0·000	0·000	0·000		
Totals	36·050	35·961	7·000	7·000	13·000	13·000	35·968	35·888	3·998	3·993	3·000	3·000	13·000	13·000	35·929	35·917	3·998	4·000	2·997	3·000	13·000	13·000

*Fe(III) and H_2O contents calculated stoichiometrically.

Table 6: Representative electron microprobe analyses of mineral phases from the Zermatt serpentinite. Ti-clinohumite and Ti-chondrodite are recalculated anhydrous, assuming full site occupancy to a total of 13 and 7 apfu, respectively

	Sample ZSG1406															
	Olivine				Antigorite				Ti-Clinohumite				Ti-Chondrodite			
SiO_2	42·21	42·12	42·11	42·42	43·57	44·53	42·57	43·35	37·90	37·88	38·13	38·75	33·85	34·22	34·66	34·81
TiO_2	0·04	0·03	0·08	0·00	0·05	0·00	0·00	0·05	2·43	3·09	2·93	2·62	7·35	7·02	7·06	7·01
Al_2O_3	0·02	0·00	0·00	0·00	1·55	1·52	1·22	1·44	0·01	0·00	0·03	0·02	0·01	0·00	0·00	0·03
Cr_2O_3	0·00	0·00	0·00	0·04	0·04	0·01	0·07	0·09	0·00	0·00	0·00	0·00	0·04	0·00	0·07	0·00
FeO	3·25	2·43	3·20	3·25	1·88	1·75	1·62	1·94	3·15	2·96	2·89	2·81	3·48	3·64	3·44	3·48
MnO	0·40	0·45	0·48	0·57	0·02	0·04	0·00	0·07	0·44	0·53	0·42	0·52	0·72	0·56	0·65	0·65
MgO	54·88	55·06	55·03	54·87	39·98	39·61	39·94	39·90	53·37	54·51	53·94	54·47	50·54	51·02	50·99	51·15
NiO	0·08	0·08	0·05	0·08	0·07	0·06	0·04	0·13	0·16	0·04	0·01	0·07	0·05	0·04	0·11	0·05
CaO	0·00	0·00	0·02	0·00	0·00	0·00	0·00	0·01	0·00	0·02	0·01	0·01	0·00	0·01	0·02	0·02
Totals	100·88	100·18	100·97	101·24	87·17	87·52	85·46	86·98	97·46	99·03	98·36	99·27	96·04	96·52	96·99	97·20
Si	0·996	0·997	0·992	0·998	2·016	2·046	2·009	2·013	4·024	3·957	4·011	4·036	2·002	2·011	2·029	2·032
Ti	0·001	0·001	0·001	0·000	0·002	0·000	0·000	0·002	0·194	0·243	0·232	0·205	0·327	0·310	0·311	0·308
Al	0·000	0·000	0·000	0·000	0·085	0·083	0·068	0·079	0·001	0·000	0·003	0·002	0·000	0·000	0·000	0·002
Cr	0·000	0·000	0·000	0·001	0·001	0·000	0·003	0·003	0·000	0·000	0·000	0·000	0·002	0·000	0·003	0·000
Fe(III)	0·000	0·000	0·001	0·000	0·000	0·000	0·000	0·000	0·000	0·000	0·000	0·000	0·000	0·000	0·000	0·000
Fe(II)	0·064	0·048	0·062	0·064	0·073	0·067	0·064	0·075	0·280	0·259	0·254	0·245	0·172	0·179	0·168	0·170
Mn	0·008	0·009	0·010	0·011	0·001	0·001	0·000	0·003	0·040	0·047	0·038	0·046	0·036	0·028	0·032	0·032
Mg	1·930	1·943	1·933	1·924	2·758	2·713	2·810	2·763	8·448	8·489	8·459	8·458	4·457	4·469	4·450	4·452
Ni	0·002	0·002	0·001	0·002	0·003	0·002	0·002	0·005	0·014	0·003	0·001	0·006	0·002	0·002	0·005	0·002
Ca	0·000	0·000	0·000	0·000	0·000	0·000	0·000	0·001	0·000	0·002	0·001	0·002	0·000	0·001	0·001	0·001
H	0·000	0·000	0·000	0·000	4·000	4·000	4·000	4·000	13·000	13·000	13·000	13·000	7·000	7·000	7·000	7·000
Totals	3·000	3·000	3·000	3·000	8·939	8·913	8·956	8·944	8·780	8·797	8·753	8·755	4·668	4·678	4·656	4·657

*Fe(III) and H_2O contents calculated stoikiometrically.

Table 7: Representative laser ablation in situ trace element analyses of mineral phases from the Cignana serpentinite. All data are reported in μg/g

	Sample ZSG1403									
	Antigorite		Ti-Clinohumite		Diopside		Olivine		Magnetite	
Li	0·0074	<0·027	2·29	3·12	0·30	0·24	2·6	1·12	1·28	0·9
Be	0·081	0·08	<0·9	<0·57	5·1	5	<0·021	<0·078	<0·29	<0·14
B	5·1	4·9	7·1	3·3	0·67	0·75	1·63	9·4	0·14	<0·063
Sc	11	9·8	4·1	3·5	25·1	23	1·25	2·13	1·71	1·9
V	48	59	20·4	27·3	5·1	5·2	0·10	0·053	930	960
Cr	2190	2270	30·8	48	68	50	1·81	1·55	39 000	32 000
Co	57	61	206	211	14·5	14·7	198	208	216	219
Ni	1120	1360	2490	2480	174	177	2830	2770	2740	2750
Cu	2·31	2·06	2·05	2·28	0·85	0·86	1·98	2·11	0·09	<0·042
Zn	46	41	123	120	8	7·8	98	99	360	247
As	0·065	0·17	<0·11	<0·091	0·032	<0·028	0·009	0·026	0·054	0·014
Rb	<0·0028	0·0028	<0·035	<0·027	<0·0073	0·011	0·0026	<0·0041	<0·0083	<0·0043
Sr	0·037	0·049	0·19	0·25	118	141	0·0015	0·012	0·092	0·036
Y	0·47	0·37	0·15	0·14	39	40	0·01	0·28	0·13	0·0056
Zr	0·11	0·16	5·4	2·86	0·19	0·19	0·0089	0·024	0·72	1·1
Nb	0·069	0·091	94	77	0·0078	0·027	0·089	0·13	0·6	0·52
Mo	0·026	0·027	0·58	0·29	<0·043	0·039	0·20	0·16	2·18	1·87
Cd	0·031	0·085	<0·25	<0·20	0·15	0·13	0·16	0·046	0·079	0·039
Sb	0·041	0·058	<0·138	<0·129	<0·038	<0·035	0·0122	0·0288	0·054	<0·0191
Cs	<0·0012	<0·0018	0·01	<0·020	<0·0049	<0·0042	<0·0016	<0·0026	<0·0059	<0·0030
Ba	<0·012	0·013	<0·11	<0·098	<0·036	<0·031	<0·0029	<0·022	0·23	<0·016
La	0·032	0·039	0·035	0·029	1·68	1·85	0·0007	0·025	0·07	0·0036
Ce	0·12	0·14	0·026	0·066	7·6	8·2	<0·0014	0·016	0·056	0·0057
Pr	0·0096	0·011	<0·018	<0·012	1·28	1·29	<0·0008	0·0042	0·0079	<0·0025
Nd	0·037	0·037	0·031	<0·057	6·3	6·2	<0·0017	0·020	0·042	0·0034
Sm	0·016	0·010	<0·074	<0·024	2·37	2·4	<0·0056	0·0035	<0·029	<0·014
Eu	0·0033	0·0039	<0·04	<0·025	0·87	0·93	<0·0006	<0·0009	0·0044	0·0014
Gd	0·028	0·018	<0·025	<0·086	3·6	3·7	<0·0073	0·0036	0·015	<0·0028
Tb	0·004	0·005	<0·010	0·0049	0·73	0·79	<0·001	<0·0013	0·0013	<0·0004
Dy	0·058	0·035	<0·059	<0·053	5·8	6·2	<0·0044	0·013	0·0071	<0·0022
Ho	0·014	0·014	0·0098	0·0069	1·37	1·45	<0·0015	0·0081	0·0037	<0·0017
Er	0·066	0·064	0·019	<0·06	4·6	4·7	<0·004	0·072	<0·023	<0·012
Tm	0·015	0·012	<0·021	0·011	0·57	0·59	0·0017	0·031	0·0014	<0·0004
Yb	0·16	0·12	0·22	0·09	3·2	3·4	0·029	0·51	<0·0089	0·0059
Lu	0·04	0·028	0·032	0·032	0·31	0·33	0·0099	0·14	<0·0047	<0·0023
Hf	0·0051	0·011	0·107	0·036	0·0083	0·0095	<0·0011	<0·0052	0·092	0·075
Ta	0·0029	0·0073	6·9	6·4	<0·0034	0·0033	0·0036	0·0061	0·046	0·044
W	0·007	<0·006	0·7	0·18	<0·014	<0·012	<0·0013	<0·0022	<0·016	<0·0076
Pb	0·020	0·0073	<0·09	<0·074	0·4	0·41	0·0079	0·0093	<0·022	<0·012
Bi	0·0069	0·019	<0·032	<0·030	<0·0094	<0·0084	0·0253	0·0043	0·0088	0·0045
Th	0·024	0·043	<0·016	<0·005	0·031	0·05	<0·0004	<0·0019	0·0064	0·0016
U	<0·0011	0·0035	<0·013	<0·012	<0·0037	0·0038	<0·0004	<0·0023	<0·0069	<0·0034

300 times PM in Nb and Ta, again consistent with the high compatibility of high field strength elements in humite–group minerals (Garrido *et al.*, 2005).

DISCUSSION

Serpentinite geochemistry: mantle protoliths and changes during serpentinization and subduction metamorphism

Numerous studies dealing with the geochemistry of oceanic and subduction-zone serpentinites have been made (Hattori & Guillot, 2003; Deschamps *et al.*, 2011; 2012; Kodolányi *et al.*, 2012; Debret *et al.*, 2013*b*; Lafay *et al.*, 2013; Scambelluri *et al.*, 2014, 2015; Cannaò *et al.*, 2015, 2016; Peters *et al.*, 2017). These demonstrate that the major element and REE compositions acquired by mantle rocks during their evolution in asthenospheric and lithospheric environments are retained after low-temperature peridotite/seawater interaction (Niu, 2004; Deschamps *et al.*, 2013), except for modification in CaO contents. This enables the distinction of partial melting and melt-rock interaction processes affecting the oceanic mantle prior to serpentinization. Being fragments of the slow-spreading Jurassic Tethys Ocean (Dal Piaz *et al.*, 2003; Piccardo, 2008; Rampone *et al.*, 2014), the mantle rocks of the Western Alpine ophiolites record superposed events of melt extraction and of peridotite re-fertilization by circulating MORB-type melts (Godard *et al.*, 2000; Dal Piaz *et al.*, 2003; Müntener *et al.*, 2004; Piccardo, 2008; Rampone *et al.*, 2014) that are still readable in the REE compositions of the Zermatt and Cignana serpentinites.

Table 8: Representative laser ablation *in situ* trace element analyses of mineral phases from Ti-chondrodite and Ti-clinohumite veins hosted in the Cignana serpentinite. All data are reported in μg/g

	Sample ZSG1402								Sample ZSG1502							
	Ti-clinohumite		Apatite		Diopside		Chlorite		Ti-clinohumite		Olivine		Antigorite		Chlorite	
Li	2·91	3·08	<0·086	<0·19	<0·66	0·48	<0·44	<0·23	4	3·3	4·9	2·81	<0·13	<0·48	<0·18	0·09
Be	<1·31	<1·68	<0·49	<0·25	3·4	4·5	<1·18	<0·61	<0·57	<1·21	<0·67	<0·38	<0·43	<1·6	<0·4	<0·25
B	2·65	2·68	0·65	1·06	<1·28	0·52	0·98	0·87	1·85	2·96	1·16	4·1	2·17	1·83	0·66	0·68
Sc	5·3	5·6	0·47	0·42	36	42	12·2	8·5	3·3	3·4	2·18	1·64	10·2	8·6	6·2	5·6
V	30·4	38	0·54	0·63	9·6	11·6	117	95	25·2	17·9	0·23	0·10	65	56	80	75
Cr	19·8	42	<2·35	<2·36	115	22·1	1050	1380	33	23	4·3	3·9	1680	1830	2520	860
Co	175	175	<0·039	0·058	15·7	14·4	67	67	188	208	223	223	75	68	76	72
Cu	2·25	10·3	<0·19	1	1·04	0·89	1·56	1·22	1·31	0·78	1·19	1·33	1·78	2·87	1·5	1·21
Zn	116	116	<0·45	<0·45	7·9	7·3	36	35	121	140	104	105	46	58	44	32
As	<0·27	<0·29	4·2	3·9	<0·28	<0·097	<0·14	0·071	<0·057	<0·12	0·36	<0·024	2·42	0·72	0·078	<0·020
Rb	<0·072	<0·083	0·27	0·27	<0·094	<0·037	<0·05	<0·025	<0·020	<0·042	<0·024	<0·013	0·093	<0·075	<0·014	<0·0092
Sr	0·65	0·7	2440	2500	170	183	0·064	0·052	0·15	0·12	0·12	0·29	0·57	0·37	0·08	0·042
Y	0·52	0·54	2270	2570	72	83	0·028	0·071	0·14	0·075	0·032	0·31	0·62	0·5	0·014	0·013
Zr	4·2	2·33	0·89	0·92	0·24	0·32	0·087	0·09	3·2	5·3	<0·020	0·13	0·85	0·28	0·046	0·082
Nb	140	190	0·89	0·47	<0·041	0·013	<0·025	0·058	14·1	13·8	0·028	0·079	0·033	<0·037	0·011	<0·0043
In	<0·029	<0·035	<0·012	<0·015	<0·026	<0·016	0·031	0·027	<0·0089	<0·019	<0·0095	<0·0054	0·015	<0·026	0·015	0·014
Sn	<0·27	0·43	<0·097	<0·095	<0·27	0·16	2·86	1·49	0·064	<0·14	<0·082	<0·043	0·14	<0·19	0·25	0·21
Sb	<0·31	<0·33	<0·11	<0·10	<0·31	<0·12	<0·15	<0·078	<0·057	<0·12	<0·059	<0·032	0·15	<0·14	<0·036	<0·023
Cs	<0·055	<0·064	<0·021	<0·022	<0·046	<0·021	<0·033	<0·017	<0·014	<0·031	<0·012	<0·0069	0·011	<0·035	<0·0074	<0·0049
Ba	0·37	0·63	<0·17	0·13	<0·39	0·12	<0·24	<0·12	<0·031	<0·067	<0·13	<0·07	0·23	<0·23	<0·076	<0·033
La	0·28	0·099	940	890	3·8	4·7	<0·041	<0·021	<0·0042	<0·009	<0·012	0·017	0·014	0·049	<0·007	<0·0055
Ce	0·61	0·22	2460	2260	17·7	19·1	<0·025	<0·013	0·0049	<0·0095	0·0069	0·036	0·085	0·16	<0·0028	<0·0046
Pr	0·037	<0·038	288	264	3·2	3·4	<0·0068	<0·0034	<0·0034	<0·0072	<0·0035	0·0027	0·011	0·032	0·0024	<0·0035
Nd	0·38	<0·21	1240	1140	19	17·9	<0·10	<0·053	<0·064	<0·17	<0·054	<0·031	0·075	0·06	<0·032	<0·025
Sm	<0·20	<0·24	304	281	7·3	6·9	<0·043	<0·022	<0·023	<0·048	<0·062	<0·036	<0·042	<0·16	<0·037	<0·023
Eu	<0·055	<0·068	50	49	1·49	1·41	<0·012	<0·0061	0·0073	<0·014	<0·007	<0·0047	<0·015	<0·057	<0·0042	<0·0027
Gd	<0·20	<0·24	360	360	9·6	10	<0·044	<0·022	<0·023	<0·048	<0·062	<0·036	<0·042	<0·158	<0·037	<0·023
Tb	<0·025	<0·031	57	55	1·65	1·81	<0·015	<0·0078	0·0034	<0·0066	<0·0033	<0·0022	0·007	<0·021	<0·0020	<0·0013
Dy	0·051	0·099	360	370	12·1	13·5	<0·023	<0·012	<0·034	<0·073	<0·014	0·034	0·056	<0·088	<0·0083	<0·0053
Ho	<0·032	<0·038	71	81	2·27	2·66	<0·016	<0·008	<0·0033	0·0077	0·0038	0·0085	0·018	0·013	<0·0021	<0·0033
Er	0·076	<0·075	204	249	6·6	8·3	<0·07	<0·036	0·027	<0·032	0·017	0·043	0·11	0·074	<0·0094	0·0088
Tm	0·020	<0·016	25·4	32	0·73	1·05	0·0061	<0·0028	<0·0081	<0·017	<0·011	0·008	0·010	<0·030	<0·0064	<0·0051
Yb	0·38	0·5	144	186	4·7	6·3	<0·096	<0·049	0·14	<0·14	0·071	0·14	0·11	<0·14	<0·033	0·021
Lu	0·11	0·10	18·1	22·7	0·52	0·66	0·013	0·022	0·019	0·038	0·036	0·028	0·035	<0·022	0·0055	0·0039
Hf	<0·087	<0·11	0·021	<0·033	<0·034	0·017	<0·068	<0·035	0·069	0·11	<0·039	<0·022	0·041	<0·03	<0·024	<0·012
Ta	7·5	12·2	0·012	0·015	<0·010	<0·021	<0·0061	<0·0031	0·72	0·79	<0·0095	<0·0055	<0·0082	<0·033	<0·0057	<0·0014
W	0·096	0·20	0·26	0·14	<0·045	<0·057	<0·11	<0·054	<0·015	<0·033	0·047	0·15	<0·014	<0·041	<0·025	<0·0061
Tl	<0·073	<0·087	<0·021	<0·027	<0·046	<0·026	<0·033	<0·017	<0·017	<0·036	<0·015	<0·0087	<0·0091	<0·033	<0·0091	<0·007
Pb	<0·13	<0·16	1·87	1·17	0·9	0·69	<0·088	<0·045	<0·046	<0·098	<0·027	<0·015	0·021	<0·078	<0·016	<0·014
Bi	<0·083	<0·096	<0·027	0·036	<0·10	<0·05	<0·05	<0·026	<0·0047	<0·01	<0·013	<0·0073	<0·012	<0·046	<0·0077	<0·006
Th	<0·085	<0·10	69	76	<0·027	0·08	<0·015	<0·008	<0·0045	<0·0096	<0·013	<0·0073	<0·0092	<0·035	<0·0076	<0·0019
U	<0·044	<0·057	10·2	16·2	<0·023	<0·025	<0·032	<0·016	<0·0042	<0·0089	<0·0045	<0·0031	<0·0069	<0·025	<0·0027	<0·0034

Table 9: Representative laser ablation *in situ* trace element analyses of mineral phases from the Zermatt serpentinite. All data are reported in μg/g

	ZSG1406							
	Serpentine			Ti-Clinohumite				
Li	<0·021	<0·011	<0·0067	0·22	0·5	1·32	0·35	<0·34
Be	<0·051	<0·044	<0·039	<0·037	<0·068	<0·077	<0·4	<0·41
B	23·3	32	9·9	22·4	21·5	18·9	1·46	0·86
Sc	12·4	12·5	11·3	14·2	29·7	65	1·03	0·85
V	25·9	25	23·2	19·5	14·8	18·2	198	203
Cr	1640	2630	530	90	60	104	4000	3500
Co	9	8·6	8·2	56	50	37	86	84
Ni	286	213	210	550	480	380	1920	1690
Cu	9·5	4·4	3·7	2·79	2·52	2·55	3·2	0·97
Zn	19·5	19·1	15·6	57	50	42	138	134
As	0·51	0·53	0·235	0·014	<0·0048	0·0078	0·051	<0·045
Rb	0·0045	<0·0031	<0·0026	<0·0026	<0·0048	<0·0041	<0·024	<0·029
Sr	0·016	0·023	0·014	0·20	0·21	0·36	0·035	0·044
Y	0·31	0·21	0·22	0·087	0·12	0·12	0·17	0·15
Zr	0·5	0·41	0·30	4·9	4·3	8·3	0·91	0·31
Nb	0·021	0·021	0·020	0·86	1·14	2·93	0·073	0·041
Mo	0·029	0·024	0·029	0·29	0·29	0·36	0·27	0·34
Cd	0·023	0·026	0·1	0·034	0·030	<0·023	<0·18	<0·23
Sb	0·17	0·17	0·096	0·012	<0·0095	<0·009	<0·064	<0·089
Cs	<0·0022	<0·0019	<0·0021	<0·0016	<0·0029	<0·0019	<0·021	<0·025
Ba	<0·011	<0·015	0·0036	0·031	<0·021	<0·0044	<0·059	0·038
La	0·006	0·0072	0·0064	0·0025	0·0010	<0·0023	<0·022	<0·025
Ce	0·020	0·015	0·019	0·0064	0·0016	<0·0020	0·033	0·021
Pr	0·0035	0·0033	0·0027	<0·0009	<0·0017	0·0005	0·011	0·005
Nd	0·015	0·021	0·020	0·010	0·0044	<0·0069	0·069	<0·065
Sm	0·012	0·011	0·0087	0·0062	<0·010	<0·0081	<0·09	<0·099
Eu	0·0032	0·004	<0·0022	<0·0016	<0·0029	<0·0009	<0·026	<0·029
Gd	0·029	0·015	0·021	0·009	0·0066	0·0034	<0·041	0·027
Tb	0·0038	0·0019	0·0049	0·0012	0·0013	<0·0012	0·0082	0·006
Dy	0·041	0·017	0·031	0·006	0·0067	0·0061	<0·032	0·027
Ho	0·011	0·0091	0·0085	0·0022	0·0025	0·0029	0·016	0·008
Er	0·043	0·019	0·031	0·0095	0·022	0·019	<0·074	<0·085
Tm	0·0055	0·0049	0·0037	0·0023	0·0054	0·0079	<0·012	<0·012
Yb	0·054	0·045	0·042	0·029	0·062	0·11	<0·041	0·035
Lu	0·013	0·0093	0·0065	0·0078	0·017	0·035	<0·0068	0·0072
Hf	0·028	0·022	0·01	0·092	0·088	0·16	0·035	<0·014
Ta	0·0008	0·0014	0·0007	0·030	0·032	0·099	<0·0068	<0·0039
W	0·0078	0·010	0·0055	0·22	0·031	0·056	0·030	0·017
Pb	0·060	0·0129	0·017	0·0066	<0·0087	<0·0089	<0·056	<0·071
Bi	0·0062	0·0053	0·027	0·017	0·0042	0·0037	<0·023	<0·027
Th	0·0017	<0·0019	0·0012	<0·0003	<0·0006	<0·0006	<0·015	<0·015
U	<0·0008	<0·0008	0·0015	0·001	0·0011	0·0014	<0·0096	<0·011

On the other hand, peridotite–seawater interaction brings about an increase in fluid-mobile B, W, U, Pb and, to a minor extent, As, Sb, which can geochemically fingerprint the serpentinization environment (Kodolányi *et al.*, 2012; Deschamps *et al.*, 2013; Cannaò *et al.*, 2016; Peters *et al.*, 2017). Exchange with seawater also causes typical variations in the Sr isotope composition of the oceanic serpentinites, which can be reset towards more radiogenic values by the interaction with crust-derived slab fluids during subduction-zone processing of these rocks (Cannaò *et al.*, 2015; Cannaò *et al.*, 2016). The REE, fluid mobile elements (FME) and isotope geochemistry of serpentinite, coupled with field and microstructural investigations, thus helps unravelling the timing and tectonic setting of fluid–rock interaction and the evolution of serpentinite.

Using this approach, we discuss the following: (1) the mantle protoliths of the Zermatt and Cignana serpentinites; (2) the possible serpentinization setting(s) and FME exchange of the Zermatt and Cignana ophiolites and the origin of the fluids interacting with the serpentinites; (3) the possible *P-T* conditions of subduction-zone metamorphism to HP–UHP conditions; and (4) the tectonic setting of the Alpine subduction zone.

The different protoliths of the Zermatt–Saas and Cignana serpentinites

Bulk-rock compositions

The higher Mg and the lower CaO and Al_2O_3 contents of the Zermatt–Saas serpentinite compared to the Cignana serpentinite (Fig. 6) point to an original difference in composition and to a different extent of partial melting and/or re-fertilization processes recorded by these

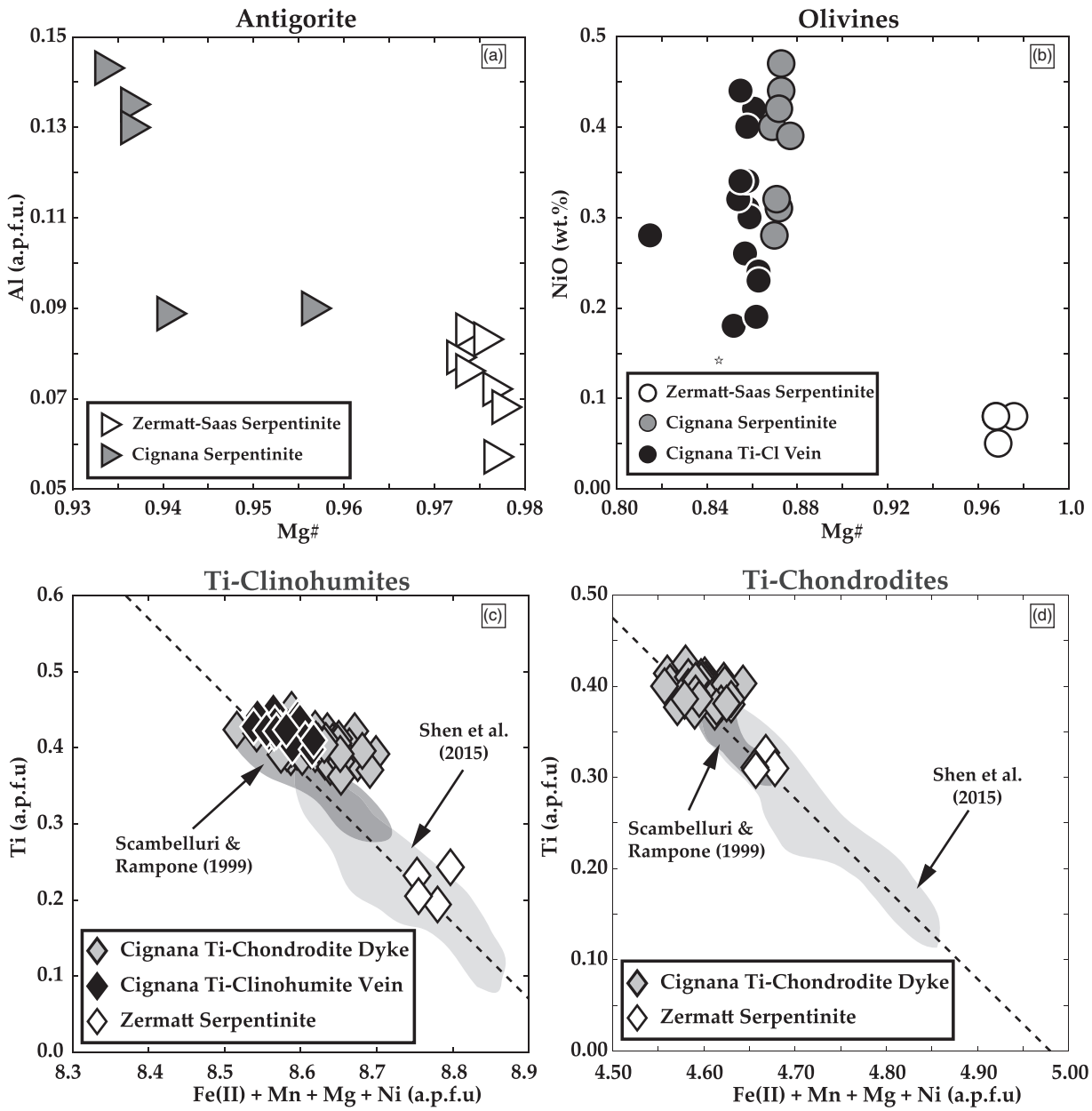

Fig. 10. Mineral analyses of serpentine, olivine, Ti-chondrodite and Ti-clinohumite from the Zermatt serpentinite, the Cignana serpentinite, and the Ti-bearing veins and dykelets. Serpentine from Zermatt has higher Mg# and lower Al content than serpentine from Cignana. Mg# in Zermatt olivine is comparable with serpentine from the same locality. Olivine from the Cignana serpentinite and Ti-clinohumite vein have similar Mg#, lower than in the Zermatt serpentinite. Note the lower Ti content of both Ti-chondrodite and Ti-clinohumite from the Zermatt serpentinite with respect to Cignana serpentinite veins.

rocks. The low CaO content of the ZSZ serpentinite with respect to the mantle depletion trend (Fig. 6) may result from Ca loss due to pyroxene dissolution and/or plagioclase chloritization during serpentinization. A duality in the protolith composition of the ZSZ and Cignana serpentinite is clearly suggested by their bulk REE compositions portrayed in Fig. 7 and showing that the LREE-depleted pattern of the ZSZ serpentinite can fit the reference compositions of harzburgite (blue field), whereas the flat REE pattern of the Cignana serpentinite overlaps the compositional range of refertilized, plagioclase-impregnated, lherzolite (orange field; Guarnieri *et al.*, 2012). The ZSZ and the Cignana serpentinites thus derive from different domains of the Tethyan oceanic lithosphere affected by melt depletion and refertilization, respectively.

Clinopyroxene composition

An origin of the Cignana serpentinite from a refertilized mantle protolith is also suggested by the REE composition of its rock-forming, metamorphic diopside. In general, the Zermatt and Cignana serpentinites do not preserve relics of mantle clinopyroxene that became overgrown by metamorphic diopside during

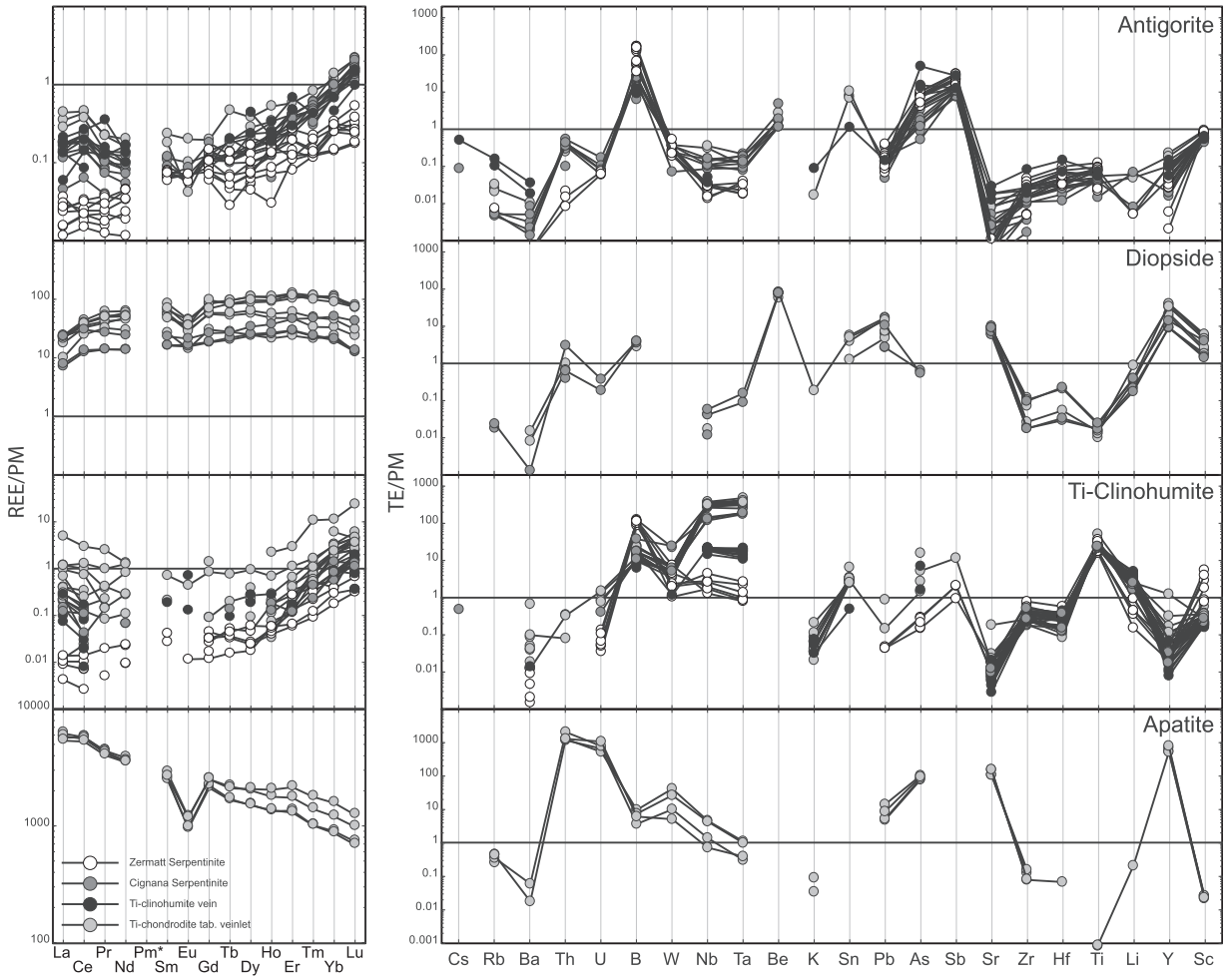

Fig. 11. REE and trace element composition of antigorite, diopside, Ti-clinohumite and apatite from the Cignana and Zermatt serpentinites.

serpentinization and subduction-zone recrystallization of these rocks. A scarcity of mantle mineral relics thus characterizes the whole Zermatt–Saas Zone (Dal Piaz *et al.*, 2003; Li *et al.*, 2004; Angiboust *et al.*, 2009; Rebay *et al.*, 2012). Nevertheless, the high REE content of metamorphic diopside from the Cignana serpentinite is compatible with the REE-rich bulk-rock composition (Fig. 7) and likely represents an inheritance from the re-fertilized mantle peridotite protolith (Guarnieri *et al.*, 2012; Rampone *et al.*, 1995). This diopside can thus help clarifying the nature of the protolith rock (Bodinier & Godard, 2007) and to envisage the fluid-mediated changes experienced by the Cignana serpentinite during its oceanic and subduction evolution. As shown in Fig. 12, the bulk Sr and Pb isotope composition of the diopside-rich bulk-rocks and the serpentine-rich, diopside-poor, layers from the Cignana serpentinite is variable: the diopside-bearing rocks plot close to MORB melts and the LCU eclogite, whereas the antigorite-rich layers follow a trend of decreasing $^{206}Pb/^{204}Pb$ and increasing $^{87}Sr/^{86}Sr$ towards Jurassic seawater compositions. This heterogeneity can be interpreted by considering that diopside and the diopside-bearing rocks still retain the composition of mantle clinopyroxene from a peridotite re-fertilized by MORB melts. Such an inherited signature was partially overprinted by interaction with seawater-derived fluids during oceanic serpentinization that caused the shift towards higher $^{87}Sr/^{86}Sr$, and lower $^{206}Pb/^{204}Pb$ reflected by the serpentine-rich layers (Fig. 12). This isotopic change was coupled with enrichment in fluid-mobile As, Sb, B, W (see Supplementary Data). An important issue outlined in Fig. 12 regards the similarity of the Sr and Pb isotopic composition of the Cignana diopside-rich rocks with MORB melts and with the Cignana eclogite, suggesting that the magma interacting with the Cignana serpentinite protolith might have been the same as that crystallizing the protolith of the Cignana eclogite. Importantly, this suggests the pre-subduction association of the crustal UHP Lago di Cignana Unit with the surrounding Cignana serpentinite.

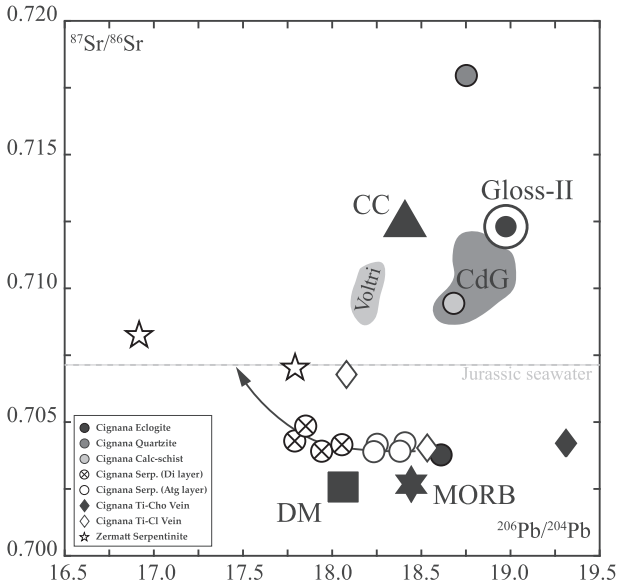

Fig. 12. $^{87}Sr/^{86}Sr$ vs $^{206}Pb/^{204}Pb$ for the analysed samples. In the Cignana serpentinites, antigorite-rich layers fall along a mixing line between the diopside-rich layers (representative of the pristine mantle imprint) and the Zermatt serpentinite (likely representative of Jurassic seawater imprint). Shaded area from Voltri (Cannaò *et al.*, 2016), Cima di Gagnone (CdG; Cannaò *et al.*, 2015). Values from GLOSS-II (Plank, 2014), depleted mantle (Rehka & Hofmann, 1997), Jurassic seawater (Jones & Jenkyns, 2001), and average continental crust (Rudnick & Gao, 2003) are reported for comparison.

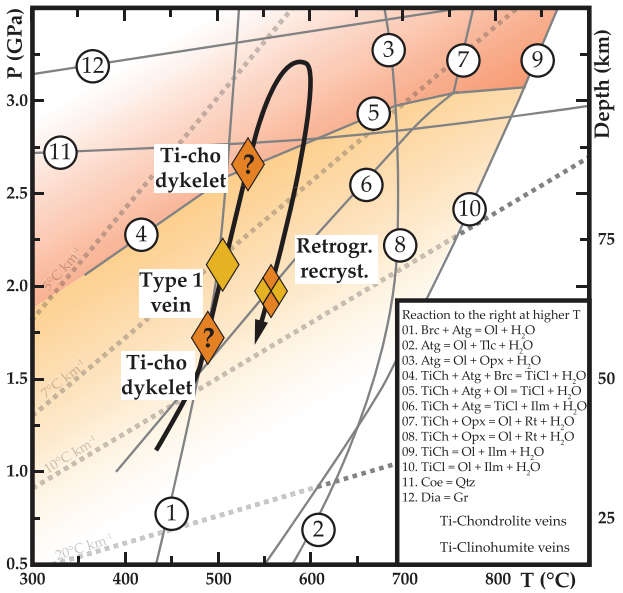

Fig. 13. Pressure–Temperature diagram showing the stability field of Ti-clinohumite (light orange) and Ti-chondrodite (dark orange) in serpentinite systems. The main reaction lines involving Ti-clinohumite and Ti-chondrodite and the quartz to coesite transition lines are from Shen *et al.* (2015). The black arrow is the PT path proposed by Groppo *et al.* (2009) for eclogites in the Lago di Cignana Unit. The dashed grey lines are the geothermal gradients for cold (5–7°C/km) and hot (20°C/km) subduction.

The Nd isotopic data (ε_{Nd} between +9 and +13; Fig. 9c) show that serpentinite still retains a mantle signature, without significant Nd addition during hydration. Nevertheless, different serpentinite samples have slightly different ε_{Nd}, consistent with a variably enriched (lower ε_{Nd} and higher Nd content) and/or depleted (higher ε_{Nd} and lower Nd content; Fig. 9c) heterogeneous mantle. The Ti-clinohumite veins have an ε_{Nd} value comparable with medium to very enriched serpentinites, suggesting that they derive from the dehydration of portions of former compositionally heterogeneous mantle rocks. This excludes a substantial involvement of sediment-derived fluids, which would have lowered the vein ε_{Nd} signature (such metasediments have negative ε_{Nd}). Instead, the higher Nd content in veins than in serpentinites derives from a higher Nd compatibility in Ti-clinohumite than in serpentine. The eclogite and the Ti-chondrodite dykelets display similar ε_{Nd} and Nd contents, suggesting a similar magma source for the Ti-chondrodite-dykelets in the Cignana serpentinite and the Cignana eclogite. In contrast, the Cignana serpentinite and the associated Ti-clinohumite veins have lower bulk Nd than the Ti-chondrodite dykelet and the Cignana eclogite. This suggests that the Ti-clinohumite veins and the Ti-chondrodite dykelet have a different origin: the latter being the metasomatic product of a former gabbroic protolith, comparable to that of the Cignana eclogite (Fig. 9c; see also Scambelluri & Rampone, 1999). This further corroborates the hypothesis of a pre-subduction association of Cignana serpentinite and the UHP Lago di Cignana Unit.

The trace element and isotopic compositions of the ZSZ and Cignana serpentinites thus point to the inheritance of compositional variations that commonly affect both present-day and fossil oceanic lithosphere (Internal Ligurides, Rampone & Piccardo, 2000; Erro–Tobbio, Rampone *et al.*, 2014; Lanzo, Müntener *et al.*, 2004; Guarnieri *et al.*, 2012). These serpentinites may thus be part of a coherent slice of oceanic lithosphere. Alternatively, the Cignana serpentinite may correspond to an independent tectonic sliver of lithospheric mantle that was detached and then juxtaposed to the ZSZ serpentinites during the Alpine subduction–exhumation cycle.

Changes during serpentinization

Zermatt serpentinite. This rock type shows positive anomalies in Bi, B, W, Sn, Pb, As, Sb, Mo with respect to the mantle depletion trend; some of these trace elements also show higher contents with respect to refertilized, plagioclase-impregnated peridotite from the Lanzo Massif (Guarnieri *et al.*, 2012). Recent work on serpentinites from present-day abyssal and fore-arc settings and from ophiolites suggests that such enrichments can equally be attributed to oceanic or to subduction zone serpentinization (Niu, 2004; Vils *et al.*, 2009; Deschamps *et al.*, 2011, 2012; Kodolányi *et al.*, 2012; Peters *et al.*, 2017). As such, the FME anomalies of the Zermatt serpentinite cannot be attributed to a

specific serpentinization environment. The prominent B enrichment, while Cs remains at peridotite levels, implies a scarce input from sedimentary reservoirs (Peters *et al.*, 2017). Moreover, no significant U uptake (acquired in serpentinite only in its oxidized state; Kodolányi *et al.*, 2012; Deschamps *et al.*, 2013; Peters *et al.*, 2017) indicates slightly less oxidised or U-depleted serpentinization fluids compared to sea water for example (Langmuir, 1978; Kodolányi *et al.*, 2012). This is further supported by W/Mo $>$ 1, since fluid-mediated Mo transport and enrichment is more redox-sensitive than for W for these otherwise geochemically very similar elements (e.g. Koschinsky & Hein, 2003; Mohajerin *et al.*, 2016). Molybdenum is thus less enriched than W in more reduced fluids (W/Mo = 0·06–0·18 for mid-ocean ridge serpentinites with U = 0·211–1·02 μg g^{-1} in Jöns *et al.*, 2010). Alternatively, W can be preferably leached from sediments into pore fluids relative to Mo (Kishida *et al.*, 2004). However, the latter process in inconsistent with the lack of Cs enrichment in the serpentinites. Overall, such fluid characteristics and resulting fluid signatures are like FME enrichment patterns observed in some ocean floor serpentinites that have been sampled in somewhat deeper parts of the lithospheric mantle exhumed at the ocean floor (Kodolányi *et al.*, 2012; Peters *et al.*, 2017).

During oceanic serpentinization, the original peridotite also exchanges isotopes with seawater. The low Pb content in seawater (Pb ~0·002 μg/g; Li, 1982) should not change significantly the Pb content of serpentinite with respect to the original peridotite (Pb ~0·05 μg/g in DM), and should not strongly change the isotopic composition of these rocks. However, as the initial Pb isotopic compositions of the pristine mantle peridotite and of Jurassic seawater are unknown, the Pb isotopic composition of the Zermatt serpentinite might be that of: (1) Jurassic seawater; (2) the pristine mantle peridotite; or 3) a mixture of the two. Regarding Sr, the bulk Sr contents of serpentinites are strongly influenced by: (1) the presence of clinopyroxene porphyroclasts, which retain most of the bulk Sr content and have a mantle isotopic imprint ($^{87}Sr/^{86}Sr$ ~0·7030–0·7040) and (2) by the amount of Sr introduced by the aqueous fluid hydrating the rock during serpentinization. As clinopyroxene is generally more resistant than olivine to serpentinization, partially serpentinized peridotites will retain most of their mantle isotopic signature and thus have a Sr isotopic composition lying on a mixing line between pristine peridotite and seawater. Since clinopyroxene clasts in the Zermatt serpentinite are scarce ($<$ 5 vol. %), the bulk isotopic composition of these rocks approximates the composition of the serpentinization fluid. As such, the $^{87}Sr/^{86}Sr$ compositions of the Zermatt serpentinites ($^{87}Sr/^{86}Sr$ = 0·707051–0·708303) imply exchange with Jurassic seawater in accordance with trace element data, without indications for further interaction with either sediment-equilibrated fluids in fore-arc regions or subduction-derived fluids along the subduction interface.

Like the bulk-rock trace element composition, the rock-forming minerals in the Zermatt serpentinite display enrichments in B, As and Sb. Antigorite displays a steady increase in HREE relative to LREE, and strong enrichments in B, As and Sb, showing a pattern compatible with oceanic serpentinization of olivine (Kodolányi *et al.*, 2012). Ti-clinohumite shows an enrichment in Nb and Ta up to PM levels, consistent with the high compatibility of high field strength elements in humite-group minerals (Garrido *et al.*, 2005). The strong B enrichment in Ti-clinohumite from HP veins suggests its preferential partitioning into this phase compared to the other vein-forming minerals, also suggested by similar bulk B values between veins and serpentinites.

In summary, the FME and the Sr–Pb isotopes suggest that the Zermatt serpentinite represents a section of an oceanic slab that was serpentinized during interaction with Jurassic seawater and still largely retains its original oceanic geochemical signature despite its Alpine subduction and exhumation history.

Cignana serpentinite. Compared with the reference refertilized plagioclase peridotite (Fig. 8), the Cignana serpentinite shows enrichments in Th, U, B, W, Nb, Ta, Be, Sn, As, Sb, Sr. However, enrichments in Th, U, Nb, Ta and Be can be ascribed to diopside that largely inherits the composition of the original mantle clinopyroxene. Boron and W are generally acquired during seafloor or fore-arc hydration and then partially lost during subduction dehydration (e.g. Peters *et al.*, 2017). Similarly to the Zermatt–Saas serpentinite, the lack of a positive Cs anomaly indicates the absence of a sedimentary or slab fluid source, and the absence of a significant fluid-enriched U component signals a less oxidizing or U-depleted serpentinization fluid. As such, the Cignana serpentinite was likely serpentinized at some depth below the seafloor.

Arsenic and Sb are generally acquired in moderate amounts during oceanic serpentinization, except for proximity to major hydrothermal sites where significant sulphide precipitation occurs (Andreani *et al.*, 2014). Moreover, several recent contributions suggest that elevated contents of As and Sb can be acquired during subduction and serpentinite emplacement in the accretionary wedge and plate interface (Hattori & Guillot, 2003, 2007; Hattori *et al.*, 2005; Deschamps *et al.*, 2011; 2012; Scambelluri *et al.*, 2014; Cannaò *et al.*, 2015, 2016). Figures 8b and c show the potential relationships between As and Sb contents of the Zermatt and Cignana serpentinites: while the As and Sb contents of the ZSZ serpentinite plot near DM and PM with enrichments up to 10 times PM (suggesting just oceanic alteration), the Cignana serpentinite displays variable increase in As and Sb with respect to ZSZ with enrichments up to 100 times PM (Fig. 8c). This enrichment can be either due to: (1) intensive oceanic hydrothermal

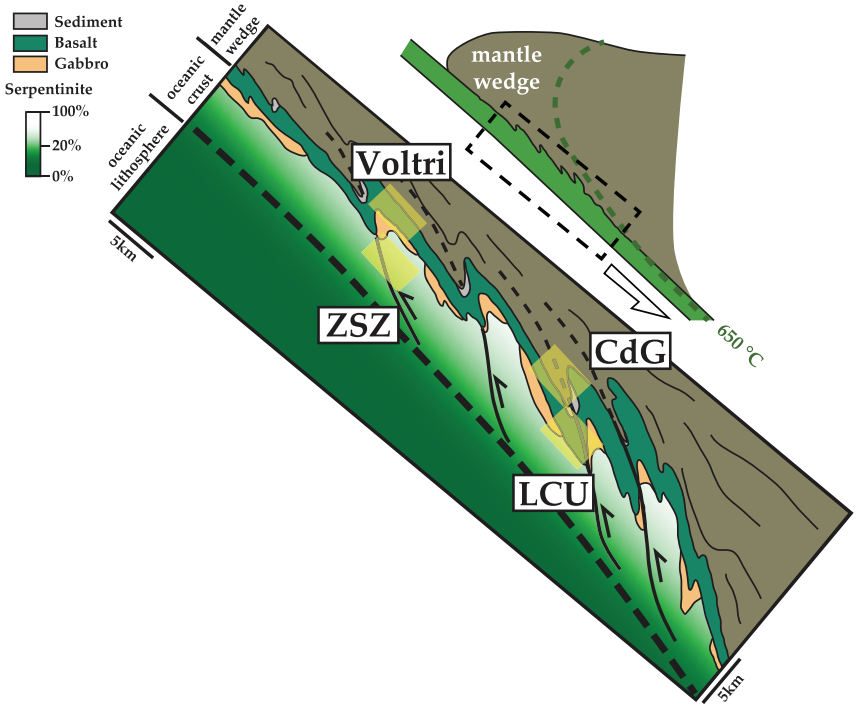

Fig. 14. Schematic cartoon illustrating the possible architecture of the cold Alpine plate interface (adapted from Guillot *et al.*, 2015). The different Alpine HP ophiolites (dashed yellow squares) accrete at different depths along the subduction plate interface. ZSZ, Zermatt–Saas Zone; LCU, Lago di Cignana Unit; CdG, Cima di Gagnone. See text for discussion.

alteration (Andreani *et al.*, 2014) or to (2) exchange with mafic crustal reservoirs during subduction (Lafay *et al.*, 2013; Scambelluri *et al.*, 2014; Cannaò *et al.*, 2015; 2016). The Cignana serpentinite shows As and Sb contents ranging towards the Lago di Cignana eclogite and metasediments, suggesting a possible exchange of these elements with such rocks during subduction or exhumation. Such an enrichment is comparable to the one recorded by other HP serpentinites (Voltri) and metaperidotites (Cima di Gagnone) for which the uptake of As and Sb via interaction of crust-derived subduction fluids has been shown on textural and geochemical grounds (Scambelluri *et al.*, 2014; Cannaò *et al.*, 2015; 2016). Assuming that Be can be another indicator of fluid exchange with sediments (Scambelluri *et al.*, 2014), the observation that the Cignana serpentinites have higher Be contents than the Zermatt Saas serpentinite supports this hypothesis.

The Sr and Pb isotope data can also be employed to trace the main serpentinization environment in Cignana. Figure 12 reports the Sr and Pb isotopic values of the ZSZ serpentinite along with the Cignana serpentinite, eclogite and metasediments. Also shown are the DM, MORB, Continental Crust, and GLOSS-II reservoirs (GLOSS-II; Plank, 2014; depleted mantle, Rehka & Hofmann, 1997; average MORB, Kelemen *et al.*, 2003; Jurassic seawater, Jones & Jenkyns, 2001; average continental crust, Rudnick & Gao, 2003). Since the Zermatt and Cignana ultramafic rocks underwent intensive serpentinization (~95 vol. %), their isotopic composition fingerprint should reflect that of the serpentinizing fluid. The overlap of Sr isotope values of the ZSZ serpentinite with Jurassic seawater ($^{87}Sr/^{86}Sr$ = 0·7070) confirms an oceanic serpentinization environment. Similarly, the Cignana serpentinite experienced oceanic serpentinization, as suggested by its B and Cs composition and by the presence of boudinaged rodingite dykes. The diopside-bearing serpentinites from Cignana preserve the original Sr and Pb mantle isotopic signature (grey circles in Fig. 12). On the other hand, the isotopic composition of serpentine-rich layers (green circles in Fig. 14a, b), though affected by the presence of minor modal diopside (about 3–5%), are better suited to define the imprint of the serpentinizing fluid. These serpentine layers plot on a mixing line between diopside layers and ZSZ serpentinite, confirming the B evidence that Cignana serpentinization was driven by seawater in an oceanic environment.

The subduction history of the Cignana serpentinite is also characterized by dehydration events, as pointed out by: (i) the occurrence of olivine + Ti-clinohumite veins, likely resulting from brucite + antigorite dehydration (about 450°C due to reaction 1, Fig. 13) and decomposition of Ti-bearing mantle clinopyroxene, according to the generalized reaction: mantle-clinopyroxene + olivine + antigorite = diopside + chlorite + Ti-clinohumite + H_2O (Lopez Sanchez-Vizcaino *et al.*, 2005). The chemical and Sr, Pb and Nd isotopic compositions of the Ti-clinohumite veins are comparable to those of the host serpentinite (Fig. 8), which suggests

that dehydration of the Cignana serpentinites was not affected by significant input of externally-derived fluids.

To conclude, the Zermatt–Saas and Cignana serpentinites largely inherit an oceanic signature represented by their Sr and Pb isotopic composition and by a characteristic enrichment in B, Mo, Cs, W and U. Such an interpretation reinforces claims made by Bretscher *et al.* (2018) who propose that even redox variations of subducted serpentinites are inherited features of heterogeneous ocean floor fluid/rock interaction. Nevertheless, minor interaction with subduction fluids sourced from the altered oceanic crust might have modified the As and Sb content of the Cignana serpentinite, leaving unaltered their Sr and Pb oceanic isotopic compositions.

Possible *P–T* evolution of the Cignana serpentinite

The subduction metamorphism of the UHP oceanic crust (eclogite and metasediments) from Cignana is well constrained in the literature (Reinecke, 1991; Reinecke, 1998; Angiboust *et al.*, 2009; Groppo *et al.*, 2009). Prograde zoning in garnet, omphacite and white mica from metasediments and eclogite points to UHP conditions of 600°C, 3·2 GPa along a cold geothermal gradient (~7°C/km; Reinecke, 1998; Rubatto *et al.*, 1998; Amato *et al.*, 1999; Groppo *et al.*, 2009; Skora *et al.*, 2015). Different from the ZSZ, the LCU records formation of coesite and microdiamond, occurring as single crystal inclusions or as fluid-related inclusions in garnet (Reinecke, 1991, 1998; Frezzotti *et al.*, 2011). Re-hydration and retrograde destabilization of the Cignana UHP minerals indicates exhumation after the UHP peak (26 km/Ma.; Amato *et al.*, 1999). The HP Zermatt–Saas serpentinites near the UHP Cignana Unit display an antigorite + olivine foliation cut by olivine + Ti–clinohumite + magnetite ± diopside metamorphic veins, formed at *P–T* conditions of 2·2–2·4 GPa and 500–550°C (Angiboust *et al.*, 2009) and 1·9–2·6 GPa and 620–650°C (Rebay *et al.*, 2012), like other Western Alpine ophiolites (Scambelluri *et al.*, 1995; Pelletier & Müntener, 2006; Debret *et al.*, 2013*a*, 2013*b*). Based on the occurrence of Ti-chondrodite in the ZSZ serpentinite, Luoni *et al.*, 2018 recently proposed that part of this unit reached UHP conditions during Alpine subduction, suggesting the ZSZ is a stack of smaller oceanic slices recording different subduction and exhumation pathways, in contrast to the view of a single, coherent tectonic unit (Angiboust *et al.*, 2009). So far, the petrology and geochemistry of serpentinites immediately surrounding the Lago di Cignana Unit (the 'Cignana serpentinites') have not been investigated in detail and these rocks are commonly attributed to the Zermatt–Saas Zone. Our data and observations of the Zermatt and Cignana serpentinites may add further evidence to this debate.

The Cignana serpentinite samples presented here record the prograde transformation of antigorite-bearing assemblages into rock- and vein-forming olivine + antigorite + Ti-clinohumite assemblages. At this stage, the olivine + Ti-clinohumite veins in the Cignana serpentinite formed in the presence of subduction fluids, as envisaged for Zermatt–Saas and other Alpine localities (Zanoni *et al.*, 2011; Rebay *et al.*, 2012; Scambelluri *et al.*, 1995; Debret *et al.*, 2013*a*). This created in the Cignana serpentinite metamorphic veins whose REE, trace element and isotopic composition mirrors that of the host-rock (Figs 7 and 8), suggesting closed-system release of 2–3 wt % water. Figure 13 shows several reaction curves (adapted from Shen *et al.*, 2015) in the system TiO_2–MgO–SiO_2–H_2O (plus the reactions graphite–diamond and quartz–coesite for comparison with the LCU crustal lithologies), which constrain the formation of the Cignana Ti-clinohumite veins at 2·0–2·5 GPa (~75 km depth), considering brucite + antigorite dehydration at about 500°C (reaction 1) and a typical Alpine subduction geothermal gradient of 6·5–7·5°C/km (Scambelluri *et al.*, 1995; Angiboust *et al.*, 2009; Groppo *et al.*, 2009).

While antigorite dehydration reactions are good temperature indicators in serpentinite, only the associated metamorphic mafic rocks (in the case of the Zermatt ophiolite, basaltic eclogite) can provide reliable pressure constraints (e.g. Angiboust *et al.*, 2009). However, recent experiments and the petrology of UHP serpentinites from Tianshan by Shen *et al.* (2015) suggests that Ti-chondrodite in serpentinites can be a viable geobarometer. According to the phase relations in Fig. 13 (Shen *et al.*, 2015), for T ~ 600°C, Ti-chondrodite forms at P > 2·7 GPa if ilmenite is absent, and at P > 2·3 GPa if ilmenite is present (see reaction 5 and 6, Fig. 13). Taking advantage of such a petrologic framework, Luoni *et al.* (2018) proposed an UHP origin for Ti-chondrodite metamorphic veins in the ZSZ serpentinite, an interpretation that might be hampered by the presence of ilmenite within these veins. Considering the Ti-chondrodite dykelets within the Cignana serpentinite presented here, Ti-chondrodite cannot be considered as an UHP marker because it hosts ilmenite inclusions which lower the Ti-chondrodite stability to ~2·3 GPa at 600°C (Fig. 13; reaction 6). However, the trace element composition of the Ti-chondrodite dykelets provides interesting hints to define the *P–T* conditions possibly reached by the Cignana serpentinite. The dykelets display REE concentrations much higher than the host rock (Fig. 7) and Nd contents like those of the Cignana eclogite (Fig. 9c). Therefore, the Cignana Ti-chondrodite dykelets likely derive from pristine differentiated, Fe–Ti-rich mafic (gabbroic?) material intruding the Cignana serpentinite (or its mantle protolith) during oceanic evolution. As described in Scambelluri & Rampone (1999), this material likely underwent early oceanic Mg-metasomatism followed by subduction-zone recrystallization to Ti-chondrodite-bearing assemblages. The close similarity in the Nd, Sr and Pb isotope composition of the Ti-chondrodite dykelet with the Cignana eclogite (Fig. 9) suggests that these rocks may be related to the same magmatic event and have been associated since the early construction stages of the

ophiolite section exposed in Cignana. Such a pristine oceanic association might have been maintained during Alpine subduction, when they reached common UHP conditions, as suggested by incoming of As and Sb into the Cignana serpentinite, and by the occurrence of UHP Ti-chondrodite in the ZSZ serpentinite nearby (Luoni *et al.*, 2018).

Therefore, we suggest that the Cignana serpentinite might have been associated with UHP crustal rocks during the oceanic and Alpine evolution. If correct, this would show that a hydrous antigorite + olivine + Ti-chondrodite paragenesis can still be stable in ultramafic systems under UHP conditions, still storing up to 10–12 wt % water (Supplementary Data).

Tectonic implications

The geochemical characteristics of ophiolitic HP serpentinites can be used to define the mantle protoliths and the oceanic alteration, as well as the eventual changes occurred during subduction-zone processing and interaction with slab fluids. As several models show (Gerya *et al.*, 2002; Angiboust *et al.*, 2012*b*), slices of oceanic lithosphere can tectonically detach from the subducting plate and accrete to the plate interface above it. Change in tectonic position can be accompanied by slab fluid influx, causing cryptic metasomatism and change in the FME and isotopic composition of serpentinite. A comparable process has been proposed for the occurrences of Cima di Gagnone (Scambelluri *et al.*, 2014; Cannaò *et al.*, 2015) and Voltri (Cannaò *et al.*, 2016) to explain enrichments in As, Sb, decrease in ^{11}B and increase in radiogenic Sr and Pb towards levels compatible with sedimentary and/or crustal reservoirs. Therefore, the apparently closed vs open system behaviour of serpentinites can shed light on their potential tectonic position within the subduction zone, whether in the slab or in the subduction interface, respectively. Our study shows that the Zermatt–Saas and the Cignana serpentinites largely retain the REE, FME and Sr isotope compositions acquired during mantle evolution and oceanic alteration. Cignana also preserves the remnants of differentiated Fe–Ti gabbroic veinlets that record oceanic metasomatism (rodingitization) causing formation of Ti-chondrodite during subduction recrystallization. These dykelets also maintain the original Nd content and Nd isotope composition of a MORB mafic rock (Fig. 9c). It appears that the ZSZ and the Cignana serpentinites essentially behaved as closed systems during subduction, apart from an increase in As and Sb in Cignana, likely due to an exchange with the associated crustal rocks.

The $^{87}Sr/^{86}Sr$ and the $^{206}Pb/^{204}Pb$ ratios of the ZSZ and Cignana serpentinites are shown in Fig. 12 in comparison with the metasomatized, plate interface ultramafic rocks from Voltri and Cima di Gagnone (Cannaò *et al.*, 2015; Cannaò *et al.*, 2016) and with reference reservoirs. In this diagram, the Sr isotope composition of the ZSZ serpentinite approximately lies on the Jurassic seawater line because of serpentinization in the oceanic environment. In contrast, the Cignana serpentinite plots on a mixing line between oceanic serpentinite, the MORB reservoir and the Cignana eclogite. This may result from a combination of MORB melt–rock reaction followed by oceanic serpentinization. A significantly different imprint affects Voltri and Cima di Gagnone, which display radiogenic Sr isotopic compositions more radiogenic than seawater along with high radiogenic Pb, plotting close to the GLOSS and continental crustal reservoirs (Fig. 12). This has been interpreted to result from exchange with slab fluids carrying radiogenic Sr and Pb acquired from crustal and sedimentary slab reservoirs (Cannaò *et al.*, 2015, 2016).

The use of radiogenic isotopes in serpentinite is a new approach to define the open vs closed geochemical behaviour of subduction-zone serpentinites, the fluid/rock exchanges and the slab fluid sources. Since fluids generally move upwards during subduction metamorphism, this way-up criterion suggests that to assimilate the crust-derived fluid signatures, the serpentinite should over-thrust, or accrete above the crustal and sedimentary rocks releasing FME and radiogenic isotopes to the fluid. Therefore, these criteria are suggested as guidelines to understand whether a subduction serpentinite evolved in a slab or in a plate interface environment, thus broadly defining the plate interface architecture and the timing of serpentinite accretion. In Fig. 14 we tentatively locate the major HP Alpine ophiolite domains along a plate interface setting: Voltri, Monviso and Cima di Gagnone significantly exchanged with subduction-zone fluids, because of accretion to the plate interface at different depths. The Zermatt–Saas Zone and the Cignana serpentinites had limited interactions with subduction fluids, being probably located in a slab setting distant from the plate interface.

CONCLUSIONS

The eclogite facies serpentinites from Valtournenche (Zermatt–Saas Zone and the serpentinite enveloping the UHP Lago di Cignana Unit) display different trace element and isotopic compositions and probably record different metamorphic histories. The bulk-rock major and trace element data show that the Zermatt and the Cignana serpentinites were derived from depleted and refertilized mantle sections of the Tethyan oceanic lithosphere, respectively. During oceanic serpentinization the mantle signatures of these rocks were overprinted by enrichment in fluid-mobile element and by the shift of the bulk-rock Sr isotope compositions towards seawater levels. This inheritance was largely preserved during the Alpine subduction and exhumation cycle, during which just a minor addition of As, Sb and Be likely occurred. Moreover, the Cignana serpentinite hosts Ti-chondrodite bearing dykelets representing the metasomatic and metamorphic recrystallization products of former differentiated gabbroic materials whose Sr and

Pb isotopic composition and Nd contents are comparable to those of eclogitized mafic crust from the UHP Lago di Cignana Unit.

The Zermatt and the Cignana serpentinites are derived from oceanic mantle sections that experienced different extents of depletion and refertilization processes within the Tethyan oceanic lithosphere. Such serpentinites may either be part of a coherent slice of oceanic lithosphere, now tectonically emplaced in the Western Alpine chain, or may correspond to independent slivers of oceanic lithosphere tectonically juxtaposed during Alpine subduction and exhumation. The similarity of the Ti-chondrodite dykelets within the Cignana serpentinite with eclogites from the UHP Lago di Cignana Unit provides geochemical evidence suggesting that these rock slices were coupled before subduction and likely shared the same *P–T* Alpine evolution.

The Sr and Pb isotopic composition of the ZSZ and of the Cignana serpentinites, when compared with those of other Alpine serpentinites, can help to unravel the possible architecture of the fossil Alpine subduction complex. If the ZSZ and Cignana serpentinites record scarce interaction with subduction zone fluids, the ultramafic rocks from other Alpine settings (e.g. Voltri and Cima di Gagnone) record significant uptake of crust and sediment-derived radiogenic Sr and Pb by interaction with slab-derived fluids. Consequently, the ZSZ and Cignana serpentinites can correspond to sections that mostly experienced closed-system behaviour during evolution in a slab environment, whereas Voltri and Gagnone experienced significant isotopic resetting due to interaction with slab-derived fluids during emplacement in plate interface settings atop the slab.

ACKNOWLEDGEMENTS

We greatly benefitted from discussions with P. Agard, E. Cannaò, H. Marschall, J. Hermann, D. Rubatto and all scientists and fellows from the ZIP project (http://www.zip-itn.eu/): discussions within ZIP stimulated this work. We thank the two anonymous reviewers, Jamie Barnes and the Editor Jörg Hermann for their comments and suggestions which helped to improve the first version of this manuscript. We also thank A. Risplendente and L. Negretti for technical assistance during the SEM and wavelength-dispersive spectrometry microprobe work.

FUNDING

M.G., M.S., T.P. and D.P. acknowledge funding by the People Programme (Marie Curie Actions, European Union's Seventh Framework Programme FP7/2007–2013) to the Initial Training Network ZIP (Zooming In-between Plates, REA grant agreement no. 604713). MG also received funding by the European Research Council (ERC) under the European Union's Horizon 2020 research and innovation programme (grant agreement No 714936 for the project TRUE DEPTHS to M Alvaro). M.S. also acknowledges support from the Italian MIUR and the University of Genova.

SUPPLEMENTARY DATA

Supplementary data are available at *Journal of Petrology* online.

REFERENCES

Abers, G. A., MacKenzie, L. S., Rondenay, S., Zhang, Z., Wech, A. G. & Creager, K. C. (2009). Imaging the source region of Cascadia tremor and intermediate-depth earthquakes. *Geology* **37**, 1119–1122.

Amato, J. M., Johnson, C. M., Baumgartner, L. P. & Beard, B. L. (1999). Rapid exhumation of the Zermatt-Saas ophiolite deduced from high-precision SmNd and RbSr geochronology. *Earth and Planetary Science Letters* **171**, 425–438.

Andreani, M., Escartin, J., Delacour, A., Ildefonse, B., Godard, M., Dyment, J., Fallick, A. E. & Fouquet, Y. (2014). Tectonic structure, lithology, and hydrothermal signature of the Rainbow massif (Mid-Atlantic Ridge 36° 14′ N). *Geochemistry, Geophysics, Geosystems* **15**, 3543–3571.

Angiboust, S., Agard, P., Jolivet, L. & Beyssac, O. (2009). The Zermatt–Saas ophiolite: the largest (60-km wide) and deepest (c. 70–80 km) continuous slice of oceanic lithosphere detached from a subduction zone? *Terra Nova* **21**, 171–180.

Angiboust, S., Agard, P., Yamato, P. & Raimbourg, H. (2012a). Eclogite breccias in a subducted ophiolite: A record of intermediate-depth earthquakes? *Geology* **40**, 707–710.

Angiboust, S., Agard, P., Raimbourg, H., Yamato, P. & Huet, B. (2011). Subduction interface processes recorded by eclogite-facies shear zones (Monviso, W. Alps). *Lithos* **127**, 222–238.

Angiboust, S., Langdon, R., Agard, P., Waters, D. & Chopin, C. (2012). Eclogitization of the Monviso ophiolite (W. Alps) and implications on subduction dynamics. *Journal of Metamorphic Geology* **30**, 37–61.

Angiboust, S., Pettke, T., De Hoog, J. C., Caron, B. & Oncken, O. (2014). Channelized fluid flow and eclogite-facies metasomatism along the subduction shear zone. *Journal of Petrology* **55**, 883–916.

Angiboust, S., Wolf, S., Burov, E., Agard, P. & Yamato, P. (2012b). Effect of fluid circulation on subduction interface tectonic processes: Insights from thermo-mechanical numerical modelling. *Earth and Planetary Science Letters* **357**, 238–248.

Bearth, P. (1967). *Die Ophiolithe Der Zone Von Zermatt–Saas Fee.* Bern: Kümmerly & Frey.

Bearth, P. & Schwandler, H. (1981). The post-Triassic sediments of the ophiolite zone Zermatt-Saas Fee and the associated manganese mineralizations. *Eclogae Geologicae Helvetiae* **74**, 189–205.

Bebout, G. E. (2007). Metamorphic chemical geodynamics of subduction zones. *Earth and Planetary Science Letters* **260**, 373–393.

Beltrando, M., Rubatto, D. & Manatschal, G. (2010). From passive margins to orogens: The link between ocean-continent transition zones and (ultra) high-pressure metamorphism. *Geology* **38**, 559–562.

Bodinier, J. L. & Godard, M. (2007). 2.04—Orogenic, Ophiolitic, and Abyssal Peridotites A2—Holland, Heinrich D. In: Turekian, K. K. (ed.) *Treatise on Geochemistry*. Oxford: Pergamon, pp. 1–73.

Bostock, M., Hyndman, R., Rondenay, S. & Peacock, S. (2002). An inverted continental Moho and serpentinization of the forearc mantle. *Nature* **417**, 536.

Bretscher, A., Hermann, J. & Pettke, T. (2018). The influence of oceanic oxidation on serpentinite dehydration during subduction. *Earth and Planetary Science Letters* **499**, 173–184.

Bucher, K. & Grapes, R. (2009). The eclogite-facies Allalin Gabbro of the Zermatt–Saas ophiolite, Western Alps: a record of subduction zone hydration. *Journal of Petrology* **50**, 1405–1442.

Bucher, K., Fazis, Y., De Capitani, C. & Grapes, R. (2005). Blueschists, eclogites, and decompression assemblages of the Zermatt–Saas ophiolite: High-pressure metamorphism of subducted Tethys lithosphere. *American Mineralogist* **90**, 821–835.

Cannaò, E., Agostini, S., Scambelluri, M., Tonarini, S. & Godard, M. (2015). B, Sr and Pb isotope geochemistry of high-pressure Alpine metaperidotites monitors fluid-mediated element recycling during serpentinite dehydration in subduction mélange (Cima di Gagnone, Swiss Central Alps). *Geochimica et Cosmochimica Acta* **163**, 80–100.

Cannaò, E., Scambelluri, M., Agostini, S., Tonarini, S. & Godard, M. (2016). Linking serpentinite geochemistry with tectonic evolution at the subduction plate-interface: The Voltri Massif case study (Ligurian Western Alps, Italy). *Geochimica et Cosmochimica Acta* **190**, 115–133.

Dal Piaz, G. (1999). The Austroalpine–Piedmont nappe stack and the puzzle of Alpine Tethys. *Memorie di Scienze Geologiche* **51**, 155–176.

Dal Piaz, G., Cortiana, G., Del Moro, A., Martin, S., Pennacchioni, G. & Tartarotti, P. (2001). Tertiary age and paleostructural inferences of the eclogitic imprint in the Austroalpine outliers and Zermatt–Saas ophiolite, western Alps. *International Journal of Earth Sciences* **90**, 668–684.

Dal Piaz, G. V. (1965). La formazione mesozoica dei calcescisti con pietre verdi fra la Valsesia e la Valtournanche ed i suoi rapporti strutturali con il ricoprimento Monte Rosa e con la Zona Sesia-Lanzo.

Dal Piaz, G. V. (1979). Manganiferus quartzitic schists of the Piemonte ophiolite nappe: In the Valsesia–Valtournanche area (Italian Western Alps).

Dal Piaz, G. V., Bistacchi, A. & Massironi, M. (2003). Geological outline of the Alps. *Episodes* **26**, 175–180.

Debret, B., Andreani, M., Godard, M., Nicollet, C., Schwartz, S. & Lafay, R. (2013). Trace element behavior during serpentinization/de-serpentinization of an eclogitized oceanic lithosphere: A LA-ICPMS study of the Lanzo ultramafic massif (Western Alps). *Chemical Geology* **357**, 117–133.

Debret, B., Nicollet, C., Andreani, M., Schwartz, S. & Godard, M. (2013). Three steps of serpentinization in an eclogitized oceanic serpentinization front (Lanzo Massif–Western Alps). *Journal of Metamorphic Geology* **31**, 165–186.

Deschamps, F., Godard, M., Guillot, S., Chauvel, C., Andreani, M., Hattori, K., Wunder, B. & France, L. (2012). Behavior of fluid-mobile elements in serpentines from abyssal to subduction environments: Examples from Cuba and Dominican Republic. *Chemical Geology* **312**, 93–117.

Deschamps, F., Godard, M., Guillot, S. & Hattori, K. (2013). Geochemistry of subduction zone serpentinites: A review. *Lithos* **178**, 96–127.

Deschamps, F., Guillot, S., Godard, M., Andreani, M. & Hattori, K. (2011). Serpentinites act as sponges for fluid-mobile elements in abyssal and subduction zone environments. *Terra Nova* **23**, 171–178.

Elter, P. & Pertusati, P. C. (1973). Considerazioni sul limite Alpi-Appennino e sulle sue relazioni con l'arco delle Alpi Occidentali: Arti grafiche Pacini Mariotti.

Forster, M., Lister, G., Compagnoni, R., Giles, D., Hills, Q., Betts, P., Beltrando, M. & Tamagno, E. (2004). Mapping of oceanic crust with" HP" to" UHP" metamorphism: The Lago di Cignana Unit, (Western Alps). Mapping geology in Italy: Geological Society of London.

Frezzotti, M., Selverstone, J., Sharp, Z. & Compagnoni, R. (2011). Carbonate dissolution during subduction revealed by diamond-bearing rocks from the Alps. *Nature Geoscience* **4**, 703.

Garrido, C. J., L., Sánchez-Vizcaíno, V., Gómez-Pugnaire, M. T., Trommsdorff, V., Alard, O., Bodinier, J. L. & Godard, M. (2005). Enrichment of HFSE in Chlorite-Harzburgite produced by high-pressure dehydration of Antigorite-Serpentinite: implications for subduction magmatism. *Geochemistry, Geophysics, Geosystems* **6**,

Gerya, T. V., Stöckhert, B. & Perchuk, A. L. (2002). Exhumation of high-pressure metamorphic rocks in a subduction channel: a numerical simulation. *Tectonics* **21**, 6-1–6-19.

Godard, M., Jousselin, D. & Bodinier, J.-L. (2000). Relationships between geochemistry and structure beneath a palaeo-spreading centre: a study of the mantle section in the Oman ophiolite. *Earth and Planetary Science Letters* **180**, 133–148.

Groppo, C., Beltrando, M. & Compagnoni, R. (2009). The P–T path of the ultra-high pressure Lago di Cignana and adjoining high-pressure meta-ophiolitic units: insights into the evolution of the subducting Tethyan slab. *Journal of Metamorphic Geology* **27**, 207–231.

Guarnieri, L., Nakamura, E., Piccardo, G. B., Sakaguchi, C., Shimizu, N., Vannucci, R. & Zanetti, A. (2012). Petrology, trace element and SR, Nd, Hf isotope geochemistry of the North Lanzo peridotite massif (Western Alps, Italy). *Journal of Petrology* **53**, 2259–2306.

Guillong, M., Meier, D. L., Allan, M. M., Heinrich, C. A. & Yardley, B. W. (2008). Appendix A6: SILLS: A MATLAB-based program for the reduction of laser ablation ICP-MS data of homogeneous materials and inclusions. *Mineralogical Association of Canada Short Course Series* **40**, 328–333.

Guillot, S., Hattori, K. H., de Sigoyer, J., Nägler, T. & Auzende, A.-L. (2001). Evidence of hydration of the mantle wedge and its role in the exhumation of eclogites. *Earth and Planetary Science Letters* **193**, 115–127.

Guillot, S., Schwartz, S., Reynard, B., Agard, P. & Prigent, C. (2015). Tectonic significance of serpentinites. *Tectonophysics* **646**, 1–19.

Hattori, K., Takahashi, Y., Guillot, S. & Johanson, B. (2005). Occurrence of arsenic (V) in forearc mantle serpentinites based on X-ray absorption spectroscopy study. *Geochimica et Cosmochimica Acta* **69**, 5585–5596.

Hattori, K. H. & Guillot, S. (2003). Volcanic fronts form as a consequence of serpentinite dehydration in the forearc mantle wedge. *Geology* **31**, 525–528.

Hattori, K. H. & Guillot, S. (2007). Geochemical character of serpentinites associated with high-to ultrahigh-pressure metamorphic rocks in the Alps, Cuba, and the Himalayas: Recycling of elements in subduction zones. *Geochemistry, Geophysics, Geosystems* **8**, 1–27.

Hermann, J., Müntener, O. & Scambelluri, M. (2000). The importance of serpentinite mylonites for subduction and exhumation of oceanic crust. *Tectonophysics* **327**, 225–238.

Ionov, D., Savoyant, L. & Dupuy, C. (1992). Application of the ICP/MS technique to trace element anaysis of peridotites and their minerals. *Geostandards and Geoanalytical Research* **16**, 311–315.

Iwamori, H. (1998). Transportation of H2O and melting in subduction zones. *Earth and Planetary Science Letters* **160**, 65–80.

Jochum, K., Seufert, H. & Thirlwall, M. (1990). Multi-element analysis of 15 international standard rocks by isotope-dilution spark source mass spectrometry. *Geostandards and Geoanalytical Research* **14**, 469–473.

John, T., Scambelluri, M., Frische, M., Barnes, J. D. & Bach, W. (2011). Dehydration of subducting serpentinite: implications for halogen mobility in subduction zones and the deep halogen cycle. *Earth and Planetary Science Letters* **308**, 65–76.

Jones, C. E. & Jenkyns, H. C. (2001). Seawater strontium isotopes, oceanic anoxic events, and seafloor hydrothermal activity in the Jurassic and Cretaceous. *American Journal of Science* **301**, 112–149.

Jöns, N., Bach, W. & Klein, F. (2010). Magmatic influence on reaction paths and element transport during serpentinization. *Chemical Geology* **274**, 196–211.

Kelemen, P., Hanghøj, K. & Greene, A. (2003). One view of the geochemistry of subduction-related magmatic arcs, with an emphasis on primitive andesite and lower crust. *Treatise on Geochemistry* **3**, 659.

Kendrick, M., Hémond, C., Kamenetsky, V., Danyushevsky, L., Devey, C. W., Rodemann, T., Jackson, M. & Perfit, M. (2017). Seawater cycled throughout Earth's mantle in partially serpentinized lithosphere. *Nature Geoscience* **10**, 222.

Kendrick, M. A., Scambelluri, M., Honda, M. & Phillips, D. (2011). High abundances of noble gas and chlorine delivered to the mantle by serpentinite subduction. *Nature Geoscience* **4**, 807.

Kienast, J.-R. (1983). Le métamorphisme de haute pression et basse température (éclogites et schistes bleus: données nouvelles sur la pétrologie des roches de la croûte océanique subductée et des sédiments associés.

Kishida, K., Sohrin, Y., Okamura, K. & Ishibashi, J-I. (2004). Tungsten enriched in submarine hydrothermal fluids. *Earth and Planetary Science Letters* **222**, 819–827.

Kodolányi, J., Pettke, T., Spandler, C., Kamber, B. S. & Gméling, K. (2012). Geochemistry of ocean floor and fore-arc serpentinites: constraints on the ultramafic input to subduction zones. *Journal of Petrology* **53**, 235–270.

Koschinsky, A. & Hein, J. R. (2003). Uptake of elements from seawater by ferromanganese crusts: solid-phase associations and seawater speciation. *Marine Geology* **198**, 331–351.

Lafay, R., Deschamps, F., Schwartz, S., Guillot, S., Godard, M., Debret, B. & Nicollet, C. (2013). High-pressure serpentinites, a trap-and-release system controlled by metamorphic conditions: Example from the Piedmont zone of the western Alps. *Chemical Geology* **343**, 38–54.

Langmuir, D. (1978). Uranium solution-mineral equilibria at low temperatures with applications to sedimentary ore deposits. *Geochimica et Cosmochimica Acta* **42**, 547–569.

Li, X. P., Rahn, M. & Bucher, K. (2004). Serpentinites of the Zermatt-Saas ophiolite complex and their texture evolution. *Journal of Metamorphic Geology* **22**, 159–177.

Li, Y.-H. (1982). A brief discussion on the mean oceanic residence time of elements. *Geochimica et Cosmochimica Acta* **46**, 2671–2675.

Lopez Sanchez-Vizcaino, V. L., Trommsdorff, V., Gomez-Pugnaire, M. T., Garrido, C. J., Muntener, O. & Connolly, J. A. D. (2005). Petrology of titanian clinohumite and olivine at the high-pressure breakdown of antigorite serpentinite to chlorite harzburgite (Almirez Massif, S. Spain). *Contributions to Mineralogy and Petrology* **149**, 627–646.

Luoni, P., Rebay, G., Spalla, M. I. & Zanoni, D. (2018). UHP Ti-chondrodite in the Zermatt-Saas serpentinite: Constraints on a new tectonic scenario. *American Mineralogist* **103**, 1002–1005.

Mahlen, N. J., Johnson, C. M., Baumgartner, L. P. & Beard, B. L. (2005). Provenance of Jurassic Tethyan sediments in the HP/UHP Zermatt-Saas ophiolite, western Alps. *Geological Society of America Bulletin* **117**, 530–544.

Marschall, H. R., Wanless, V. D., Shimizu, N., von Strandmann, P. A. P., Elliott, T. & Monteleone, B. D. (2017). The boron and lithium isotopic composition of mid-ocean ridge basalts and the mantle. *Geochimica et Cosmochimica Acta* **207**, 102–138.

McArthur, J. M., Howarth, R. & Bailey, T. (2001). Strontium isotope stratigraphy: LOWESS version 3: best fit to the marine Sr-isotope curve for 0–509 Ma and accompanying look-up table for deriving numerical age. *The Journal of Geology* **109**, 155–170.

McDonough, W. F. & Sun, S.-S. (1995). The composition of the Earth. *Chemical Geology* **120**, 223–253.

Meija, J., Coplen, T. B., Berglund, M., Brand, W. A., De Bièvre, P., Gröning, M., Holden, N. E., Irrgeher, J., Loss, R. D., Walczyk, T. & Prohaska, T. (2016). Isotopic compositions of the elements 2013 (IUPAC technical Report). *Pure and Applied Chemistry* **88**, 293–306.

Mohajerin, T. J., Helz, G. R. & Johannesson, K. H. (2016). Tungsten–molybdenum fractionation in estuarine environments. *Geochimica et Cosmochimica Acta* **177**, 105–119.

Müntener, O., Pettke, T., Desmurs, L., Meier, M. & Schaltegger, U. (2004). Refertilization of mantle peridotite in embryonic ocean basins: trace element and Nd isotopic evidence and implications for crust–mantle relationships. *Earth and Planetary Science Letters* **221**, 293–308.

Niu, Y. (2004). Bulk-rock major and trace element compositions of abyssal peridotites: implications for mantle melting, melt extraction and post-melting processes beneath mid-ocean ridges. *Journal of Petrology* **45**, 2423–2458.

Pelletier, L. & Müntener, O. (2006). High-pressure metamorphism of the Lanzo peridotite and its oceanic cover, and some consequences for the Sesia–Lanzo zone (northwestern Italian Alps). *Lithos* **90**, 111–130.

Peters, D., Bretscher, A., John, T., Scambelluri, M. & Pettke, T. (2017). Fluid-mobile elements in serpentinites: Constraints on serpentinisation environments and element cycling in subduction zones. *Chemical Geology* **466**, 654–666.

Peters, D. & Pettke, T. (2017). Evaluation of Major to Ultra Trace Element Bulk Rock Chemical Analysis of Nanoparticulate Pressed Powder Pellets by LA-ICP-MS. *Geostandards and Geoanalytical Research* **41**, 5–28.

Pettke, T., Oberli, F., Audétat, A., Guillong, M., Simon, A. C., Hanley, J. J. & Klemm, L. M. (2012). Recent developments in element concentration and isotope ratio analysis of individual fluid inclusions by laser ablation single and multiple collector ICP-MS. *Ore Geology Reviews* **44**, 10–38.

Piccardo, G. (2008). The Jurassic Ligurian Tethys, a fossil ultra-slow-spreading ocean: the mantle perspective. *Geological Society, London, Special Publications* **293**, 11–34.

Plank, T. (2014). The chemical composition of subducting sediments. *Treatise on Geochemistry* **4**, 607–629.

Rampone, E., Borghini, G., Romairone, A., Abouchami, W., Class, C. & Goldstein, S. L. (2014). Sm–Nd geochronology of the Erro-Tobbio gabbros (Ligurian Alps, Italy): insights into the evolution of the Alpine Tethys. *Lithos* **205**, 236–246.

Rampone, E., Hofmann, A., Piccardo, G., Vannucci, R., Bottazzi, P. & Ottolini, L. (1995). Petrology, mineral and isotope geochemistry of the External Liguride peridotites (Northern Apennines, Italy). *Journal of Petrology* **36**, 81–105.

Rampone, E. & Piccardo, G. B. (2000). The ophiolite-oceanic lithosphere analogue: new insights from the Northern Apennines (Italy.). *Special Papers-Geological Society of AMERICA* 21–34.

Rebay, G., Spalla, M. & Zanoni, D. (2012). Interaction of deformation and metamorphism during subduction and exhumation of hydrated oceanic mantle: insights from the Western Alps. *Journal of Metamorphic Geology* **30**, 687–702.

Rebay, G., Zanoni, D., Langone, A., Luoni, P., Tiepolo, M. & Spalla, M. I. (2018). Dating of ultramafic rocks from the Western Alps ophiolites discloses Late Cretaceous subduction ages in the Zermatt-Saas Zone. *Geological Magazine* **155**, 298–315.

Reddy, S., Wheeler, J. & Cliff, R. (1999). The geometry and timing of orogenic extension: an example from the Western Italian Alps. *Journal of Metamorphic Geology* **17**, 573–590.

Rehka, M. & Hofmann, A. (1997). Recycled ocean crust and sediment in Indian Ocean MORB. *Earth and Planetary Science Letters* **147**, 93–106.

Reinecke, T. (1991). Very-high-pressure metamorphism and uplift of coesite-bearing metasediments from the Zermatt-Saas zone, Western Alps. *European Journal of Mineralogy* **3**, 7–18.

Reinecke, T. (1998). Prograde high-to ultrahigh-pressure metamorphism and exhumation of oceanic sediments at Lago di Cignana, Zermatt-Saas Zone, western Alps. *Lithos* **42**, 147–189.

Reynard, B. (2013). Serpentine in active subduction zones. *Lithos* **178**, 171–185.

Ribeiro, J. M. & Lee, C.-T A. (2017). An imbalance in the deep water cycle at subduction zones: the potential importance of the fore-arc mantle. *Earth and Planetary Science Letters* **479**, 298–309.

Rubatto, D., Gebauer, D. & Fanning, M. (1998). Jurassic formation and Eocene subduction of the Zermatt–Saas-Fee ophiolites: implications for the geodynamic evolution of the Central and Western Alps. *Contributions to Mineralogy and Petrology* **132**, 269–287.

Rudnick, R. L. & Gao, S. (2003). Composition of the continental crust. *Treatise on Geochemistry* **3**, 659.

Rüpke, L. H., Morgan, J. P., Hort, M. & Connolly, J. A. (2004). Serpentine and the subduction zone water cycle. *Earth and Planetary Science Letters* **223**, 17–34.

Ryan, J. G. & Chauvel, C. (2013). The subduction-zone filter and the impact of recycled materials on the evolution of the mantle.

Savov, I. P., Ryan, J. G., D'Antonio, M., Kelley, K. & Mattie, P. (2005). Geochemistry of serpentinized peridotites from the Mariana Forearc Conical Seamount, ODP Leg 125: implications for the elemental recycling at subduction zones. *Geochemistry, Geophysics, Geosystems* **6**, 1–24.

Scambelluri, M., Cannaò, E. & Gilio, M. (2019). The water and fluid-mobile element cycles during serpentinite subduction. A review. *European Journal of Mineralogy* **31**, doi: 10.1127/ejm/2019/0031-2842.

Scambelluri, M., Fiebig, J., Malaspina, N., Müntener, O. & Pettke, T. (2004). Serpentinite subduction: implications for fluid processes and trace-element recycling. *International Geology Review* **46**, 595–613.

Scambelluri, M., Müntener, O., Hermann, J., Piccardo, G. B. & Trommsdorff, V. (1995). Subduction of water into the mantle: history of an Alpine peridotite. *Geology* **23**, 459–462.

Scambelluri, M., Müntener, O., Ottolini, L., Pettke, T. T. & Vannucci, R. (2004). The fate of B, Cl and Li in the subducted oceanic mantle and in the antigorite breakdown fluids. *Earth and Planetary Science Letters* **222**, 217–234.

Scambelluri, M., Pettke, T. & Cannaò, E. (2015). Fluid-related inclusions in Alpine high-pressure peridotite reveal trace element recycling during subduction-zone dehydration of serpentinized mantle (Cima di Gagnone, Swiss Alps). *Earth and Planetary Science Letters* **429**, 45–59.

Scambelluri, M., Pettke, T., Rampone, E., Godard, M. & Reusser, E. (2014). Petrology and trace element budgets of high-pressure peridotites indicate subduction dehydration of serpentinized mantle (Cima di Gagnone, Central Alps, Switzerland). *Journal of Petrology* **55**, 459–498.

Scambelluri, M. & Rampone, E. (1999). Mg-metasomatism of oceanic gabbros and its control on Ti-clinohumite formation during eclogitization. *Contributions to Mineralogy and Petrology* **135**, 1–17.

Scambelluri, M. & Tonarini, S. (2012). Boron isotope evidence for shallow fluid transfer across subduction zones by serpentinized mantle. *Geology* **40**, 907–910.

Schwartz, S., Allemand, P. & Guillot, S. (2001). Numerical model of the effect of serpentinites on the exhumation of eclogitic rocks: insights from the Monviso ophiolitic massif (Western Alps). *Tectonophysics* **342**, 193–206.

Shen, T., Hermann, J., Zhang, L., Lü, Z., Padrón-Navarta, J. A., Xia, B. & Bader, T. (2015). UHP metamorphism documented in Ti-chondrodite-and Ti-clinohumite-bearing serpentinized ultramafic rocks from Chinese southwestern Tianshan. *Journal of Petrology* **56**, 1425–1458.

Skora, S., Mahlen, N., Johnson, C. M., Baumgartner, L. P., Lapen, T., Beard, B. L. & Szilvagyi, E. (2015). Evidence for protracted prograde metamorphism followed by rapid exhumation of the Zermatt-Saas Fee ophiolite. *Journal of Metamorphic Geology* **33**, 711–734.

Spandler, C., Hammerli, J. & Pirard, C. (2018). Neodymium isotope disequilibria in subducted sediments, and potential consequences for subduction-zone recycling. *Geology* **46**, 815–818.

Spandler, C. & Pirard, C. (2013). Element recycling from subducting slabs to arc crust: A review. *Lithos* **170**, 208–223.

Tanaka, T., Togashi, S., Kamioka, H., Amakawa, H., Kagami, H., Hamamoto, T., Yuhara, M., Orihashi, Y., Yoneda, S., Shimizu, H., Kunimaru, T., Takahashi, K., Yanagi, T., Nakano, T., Fujimaki, H., Shinjo, R., Asahara, Y., Tanimizu, M. & Dragusanu, C. (2000). JNdi-1: a neodymium isotopic reference in consistency with LaJolla neodymium. *Chemical Geology* **168**, 279–281.

Todt, W., Cliff, R. A., Hanser, A. & Hofmann, A. (1996). Evaluation of a 202Pb–205Pb Double Spike for High-Precision Lead Isotope Analysis. *Earth Processes: reading the Isotopic Code* 429–437.

Ulmer, P. & Trommsdorff, V. (1995). Serpentine stability to mantle depths and subduction-related magmatism. *Science* **268**, 858–861.

Vils, F., Tonarini, S., Kalt, A. & Seitz, H.-M. (2009). Boron, lithium and strontium isotopes as tracers of seawater–serpentinite interaction at Mid-Atlantic ridge, ODP Leg 209. *Earth and Planetary Science Letters* **286**, 414–425.

Weber, S. & Bucher, K. (2015). An eclogite-bearing continental tectonic slice in the Zermatt–Saas high-pressure ophiolites at Trockener Steg (Zermatt, Swiss Western Alps). *Lithos* **232**, 336–359.

Zanoni, D., Rebay, G. & Spalla, M. (2016). Ocean floor and subduction record in the Zermatt-Saas rodingites, Valtournanche, Western Alps. *Journal of Metamorphic Geology* **34**, 941–961.

Zanoni, D., Rebay, G., Spalla, M. I. & Bernardoni, J. (2011). Eclogitised rodingites of the Zermatt-Saas Zone: unravelling their evolution through deformation–metamorphism relationships. *Rendiconti Online Societa Geologica Italiana* **15**, 131–134.